5-2008

Structural basis of bilayer deformation by membrane-associated scaffolds

Adam Frost
Yale University.

ABSTRACT

Structural Basis of Bilayer Deformation by Membrane-Associated Scaffolds

Adam Frost

Yale University

2008

The assembly of amphipathic lipids into fluid bilayers that are impermeable to macromolecules is fundamental to the existence of viruses, organelles, and cells. Conversely, membrane compartmentalization poses problems, since essential processes like cell division, cell migration, endo-, exo-, and transcytosis all require cells to remodel and even break their membranes without opening lethal leaks. Evolutionary forces have consequently generated proteins that can reversibly mold membranes into planes, spheres, cylinders, and saddle-shaped surfaces. Principally, the BAR (Bin, Amphiphysin, RVS) domain superfamily of proteins are recruited from the cytoplasm to induce or stabilize states of high membrane curvature, while the Dynamin superfamily of 'large GTPases' facilitate the fission of various vesicles and organelles. Members of the BAR domain superfamily often work in concert with members of the Dynamin superfamily to form and then fission membrane tubules. Here, we describe the membrane deforming properties of select F-BAR modules and the GTPase dynamin-1 that were discovered though reconstitution and direct visualization of these proteins as they shape and break model membranes.

Structural Basis of Bilayer Deformation by Membrane-Associated Scaffolds

A Dissertation

Presented to the Faculty of the Graduate School

of Yale University

In Candidacy for the Degree of

Doctor of Philosophy

By

Adam Frost

Dissertation Director: Vinzenz M. Unger

May 2008

Acknowledgements

As I prepare to return to medical school, I admit I see a tunnel at the end of all the light that has been my graduate training. These five years have been among the best and most transformative years of my life, and I am grateful to many people for their positive influences on me.

First, my outstanding thesis advisor, Vinzenz Unger, whose generosity as a mentor is unmatched. His door was always open and he seemd to be eagerly waiting for me to barge in and bounce ideas off his brain. His supply of chocolate and champagne was always there, ready to greet both dissappointment and accomplishment. Vinzenz managed to be deeply committed to my success in the lab and simultaneously willing to let me learn from failure as I explored (a lot of) blind alleys and insisted on doing things my (usually wrong-headed) way. Thank you, Vinzenz.

Second, my co-mentor and close collaborator, Pietro De Camili. I often felt like all I had to do was stand up and ride the wave of his enthusiasm and encouragement. To say that his influence was a driving force fails to capture how much fun working with him was. Thank you, Pietro.

Fred Sigworth was on my thesis committee and my qualifying committee. I am still working on my homework assignment to prove that the Inverse Fourier Transform of the Contrast Transfer Function yields the Fresnel Propagator Integral for a wavefront in free space; thank you for all of those hours Fred. Stephen Strittmatter was on my thesis committee and he was always insightful in suggesting experiments, the negative results of which may or may not be found in the following pages. David Chester gave me invaluable

advice with wide angle X-ray scatter experiments; and he always got a laugh out of me with his homemade "Holy Carbon" joke.

I would be remiss to leave out my colleagues and labmates: Kraimir Spasov, Thomas Marlovits, Stephen Aller, Matthew Swanson, Edward Eng, Christopher Defeo, Matthew Roberts, Sara Mootien, Adrien Flores, and Carsten Mim: thank you for protecting me from the sphere of death hidden within the negation field, and for sharing the many fine things that fermenting *Pichia* and *Saccharomyces* can provide. A big thanks in particular to my co-authors, Aurélien Roux, Rushika Perera, Krasimir Spasov, Olivier Destaing, and Edward H. Egelman; outstanding scientists, but also good friends. Edward Egelman gave me a conceptual map when I was mired in the wasteland of helical reconstruction, and Aurélien Roux was the wizard behind the dynamin chapter of this story. Rushika Perera's post-doctoral advisor, Derek Toomre, generously provided resources and advice for the live cell imaging experiments; and Bridget Carragher and the staff at the National Resource for Automated Molecular Microscopy helped with me collect the high resolution data. Robert Bjornson and Nicholas Carriero at the Yale Center for High Performance Computation in Biology and Biomedicine pulled me out of more than one programming mire. Finally, the Epilepsy Foundation generously supported me with a pre-doctoral research training fellowship, even though one reviewer of my proposal said the project had essentially nothing to do with epilepsy (and wondered why we weren't doing cryo-EM of whole brains).

My parents and sisters kept me down to earth, while my grandmothers kept on being proud. Above all, Tiffany Lundeen—with whom I am celebrating our 10-year wedding anniversary this year—encouraged, supported and loved me through the daily roller coaster of becoming a scientist. She didn't always want to hear *all* the details, but she was always happy to see me excited and willing to give me an extra kiss when I was less-than-excited.

Thank you, Tiffany. Our daughter, Heron, just turned two and it seems like she'll be able to read and understand most of my thesis by the time she turns three. I hope when she does read it that she knows how deeply I love her and how happy I am when I am with her. Before I stand up to defend this thesis in public (but hopefully not before I finish writing it...) our second child, Azure, will have been born. This thesis is dedicated to Heron and Azure, in the hope that the years spent working on this project will help me get a real job!

Table of Contents

List of Figures and Tables

Chapter 1: Introduction

Membrane Remodeling: The Next Frontier of Structural Biology

Vast and largely unexplored, the interfaces between biological membranes and the compartments they delimit are the loci of diverse and essential processes, including cellular motility, intra- and inter-cellular communication, cell division, and the biogenesis of organelles. Great strides have been made in characterizing membrane dynamics, but a mechanistic understanding of these processes remains in its infancy. Missing from the analysis to date are structural descriptions of membrane-associated macromolecules and their interactions with the bilayer. To advance our understanding of these fundamental mechanisms, we have exploited the versatility of (cryo)electron microscopy to directly image membrane-bound protein modules whose interactions with the bilayer are critical players in membrane remodeling processes.

The BAR Domain Superfamily

The BAR (Bin, Amphiphysin, Rvs) domain superfamily of proteins have emerged as important actors in membrane-remodeling processes throughout eukarya. Members of the superfamily are recruited from the cytoplasm to trigger the formation of plasma membrane extensions, invaginations, tubular organelles and transport intermediates, including endocytic vesicles (Itoh et al., 2005; Kamioka et al., 2004; Lee et al., 2002; Mattila et al., 2007; Peter et al., 2004; Tsujita et al., 2006). Within the BAR domain superfamily, a unique subset of proteins that possess F-BAR (Fes/CIP4 homology-BAR) domains have been shown to play key roles in membrane and cytoskeletal remodeling, coupling these processes by simultaneously bending bilayers and triggering the polymerization of actin fibers (Chitu and Stanley, 2007). The F-BAR subset is also notable for the number of mutations in different F-

BAR proteins that are associated with metabolic, auto-inflammatory, neurological, and malignant diseases (Chitu and Stanley, 2007). Here, we will review how F-BARs compare structurally within the BAR domain superfamily and the proposed molecular mechanisms by which they mold membranes.

With more than 14 near-atomic structures of BAR domains, we can begin generalizing about their form, function and evolutionary history (Casal et al., 2006; Gallop et al., 2006; Henne et al., 2007; Li et al., 2007; Masuda et al., 2006; Mattila et al., 2007; Millard et al., 2005; Peter et al., 2004; Pylypenko et al., 2007; Shimada et al., 2007; Tarricone et al., 2001; Weissenhorn, 2005; Zhu et al., 2007). The first structure solved, residues 118-341 of human Arfaptin-2, was not immediately recognized as the founding member of the BAR domain family (Tarricone et al., 2001). In fact, Arfaptin's ability to induce membrane-curvature was not discovered until the second structure, residues 26-242 of *Drosophila* Amphiphysin, was shown to be Arfaptin's structural homolog and their common quaternary fold was proposed to be "a universal and minimal BAR domain...a dimerization, membrane-binding, and curvature-sensing module" (Peter et al., 2004). The shared features of these two structures have proven to be defining elements of the BAR superfamily: monomers with three α-helices arranged in anti-parallel coiled-coils that dimerize to form curved modules with a positively-charged surface. Like the three-helix bundles of the spectrin superfamily (Parry et al., 1992), combinations of 3-plus-4 spacing between hydrophobic residues appears to drive the assembly of BAR monomers into coiled-coils (Chothia et al., 1981; Kumar and Bansal, 1996). The dimerization interface between BAR monomers is composed of mixed hydrophobic and polar surfaces that are buried where stretches of the α-helices from one monomer pack against those of the other monomer in an anti-parallel orientation. The surface area involved in dimerization varies more than 2-fold between individual structures,

and a major unanswered question is whether most BARs form constitutive dimers or whether dimerization can be a regulated event that occurs in the cytosol or on the membrane surface (Gallop et al., 2006; Henne et al., 2007; Li et al., 2007; Pylypenko et al., 2007; Shimada et al., 2007). While many interesting differences exist between individual BAR modules, architectural conservation of the dimeric 6-helix bundle is the touchstone of the BAR domain superfamily.

Fig. 1-1: The BAR Domain Superfamily

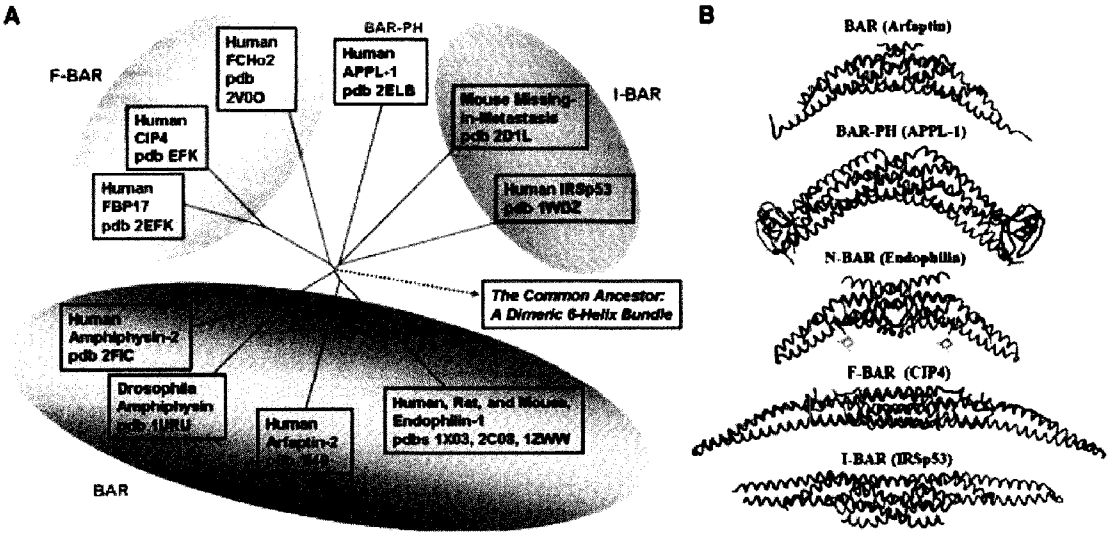

A) Phylogenetic tree of the BAR domain superfamily computed with KALIGN (Lassmann and Sonnhammer, 2005; Lassmann and Sonnhammer, 2006). Parameters used in the calculation: Gap open penalty = 11.0, Gap extension penalty = 1.5, Terminal gap penalties = 0.20, and Bonus score = 0.0 (B) Comparative views of representative members of the BAR superfamily. In the case of the N-BAR domain, the N-terminal amphipathic helix is not part of the crystal structure and is shown as a schematic only (Gallop et al., 2006).

Adapted for Diverse Membrane-Molding Mechanisms

Shifting our focus from the center of the 6-helix bundle toward the dimer's twin-tips, the distinctive adaptations of individual domains become apparent and some intuitive concepts about the mechanisms by which BARs mold membranes suggest themselves. The BAR of Arfaptin serves as the founding and paradigmatic example of a "classical" banana-shaped BAR module, characterized by a concave surface with positive charges aligned to interact with the negative charges of the membrane. Just looking at this structure leads one to the "scaffolding" hypothesis, which posits that these modules bend membranes by simply imposing their charged, curved shapes via electrostatic attraction (Itoh and De Camilli, 2006; Peter et al., 2004). Closely related to Arfaptin in their degree of curvature, the BARs of amphiphysin and endophilin are distinctive in that they are flanked by N-terminal sequences of ~26 residues that appear to fold into α-helices (the so called "Helix 0") in the interfacial environment of the bilayer (Farsad et al., 2001; Gallop et al., 2006). The intercalation of these amphipathic α-helices into the bilayer has been proposed to act like a "wedge" that causes local "buckling" when the lipid's polar headgroups of one monolayer are pushed apart (Zimmerberg and Kozlov, 2006). Biochemical (Farsad et al., 2001; Henne et al., 2007) and spectroscopic (Gallop et al., 2006) data indicate that the N-terminal helix of endophilin and amphiphyisn do act like "wedges" that penetrate into the outer region of one membrane leaflet, acting synergistically with the shape-based scaffolding properties of the BAR module. Peter *et al.* dubbed the combination of a BAR plus an N-terminal amphipathic helix the N-BAR module, and these proteins appear to constitute a discrete phylogenetic subset of the BAR domain superfamily (Frost et al., 2007; Peter et al., 2004).

Like the N-BAR domains described above, there are additional examples of BAR domain superfamily modules that have co-evolved with conjoined lipid-binding motifs,

including PH (Plecksrin Homology) and PX (Phox Homology) domains. Structural examples of these conjunctions include the BAR-PH module of APPL-1 (Li et al., 2007) and the PX-BAR module of the SNX9 (Pylypenko et al., 2007). In the case of the BAR-PH structure, an acute angle of dimerization produces the most highly-curved, "boomerang" shape of the known BAR structures. This geometry positions the phospholipid binding site of the PH domain (found at the dimers twin-tips) in line with the membrane-binding surface of the BAR domain, strongly suggesting that the conjoined domains act together to recognize specific phosphorylated phosphatidyl-inositides, while scaffolding a very high degree of membrane curvature. Similar principles apply to the PX-BAR structure of SNX9, though in this case the N-terminal PX domains appear to be more flexibly coupled to the lateral surface of the BAR core by a split "yoke" sub-domain (Pylypenko et al., 2007). In addition, an amphipathic sequence found immediately N-terminal to the PX-BAR domain appears to function like the N-terminal amphipathic "Helix 0" of amphiphysin and endophilin (Pylypenko et al., 2007).

Though only distantly homologous in primary sequence, I-BAR (Inverse-BAR) domains are also descendents of an elongated, dimeric six-helix bundle and are characterized by a surface with positive charges aligned to interact with the negative charges of the membrane (Habermann, 2004; Lee et al., 2007; Mattila et al., 2007; Millard et al., 2005). Like the BAR domain of Arfaptin, I-BAR domains also bind to Rac GTPases (Suetsugu et al., 2006; Tarricone et al., 2001). However, I-BARs are found in the proteins IRSp53 (Insulin Receptor Substrate) and MIM (Missing-In-Metastasis; or IMD for IRSp53, MIM homology Domain) and—having nearly neutral curvature—have been described as "zeppelin" shaped (Suetsugu et al., 2006). The moniker I-BAR is particularly appropriate because these domains appear to induce the formation of filopodia or plasma membrane extensions by through an

"inverse" scaffolding mechanism that generates negative—rather than positive—membrane curvature through imposition of the dimer's cationic and convex surface (Mattila et al., 2007).

F-BAR domains, the most recently adopted members of the BAR superfamily, were found via sequence searches for regions of low sequence homology to BAR domains but with secondary structure predictions consistent with three-helix, anti-parallel coiled-coils (Itoh et al., 2005; Peter et al., 2004). An entire family of actin-regulatory proteins with such homology was already known as FCH (Fes and CIP4 Homology) proteins (Aspenstrom, 1997) or as PCH (S. pombe Cdc15 Homology) proteins (Chitu and Stanley, 2007; Lippincott and Li, 2000). Extensive biochemical and cell biological analyses support the hypothesis that these regions are functional and structural relatives of the BAR domain and the names F-BAR (FCH-BAR) or EFC (Extended-FCH) were accordingly proposed (Itoh et al., 2005; Tsujita et al., 2006). New structures solved by Shimada *et al.* and Henne *et al.* validated this hypothesis, providing structural, spectroscopic and biochemical evidence that the F-BAR modules of FBP17, CIP4 and FCHo2 are α-helical, anti-parallel dimers with a conserved 6-helix bundle core but with arc depths ~3-fold smaller than those of "classical" BARs (Henne et al., 2007; Shimada et al., 2007). The more subtle curvature correlates directly with the larger diameter membrane tubules formed by F-BAR versus N-BAR domains *in vitro* (Henne et al., 2007; Itoh et al., 2005; Shimada et al., 2007).

F-BARs are also unique among the BAR domain superfamily in their possession of five α-helices, where their first and fifth helices are very short and α1 of one monomer interacts with α5 of the adjacent monomer to contribute to dimer formation. Furthermore, F-BAR monomers have "an extended C-terminal peptide" that interacts with α3 and α4 of

the adjacent monomer, all together doubling the surface area buried by dimerization (Henne et al., 2007; Shimada et al., 2007). Accordingly, Shimada *et al.* find that the F-BAR domains of human CIP4 and FBP17 are constitutive dimers, whereas Henne *et al.* report that after deleting the c-terminal peptide FCHo2 dimers become relatively weak, with a K_d on the order of dissociation constants reported by the McMahon group for other "classical" BAR domains (~2.5 μM versus 2–15 μM; Henne et al., 2007; Gallop et al., 2006). Biologically, this suggests that the extended C-terminal peptide is an important functional component of the F-BAR domain and highlights the open questions about whether dimerization is a regulated step for some members of the superfamily.

Beyond its role in dimerization, the C-terminal extended peptide may be a critical component of F-BAR function through its role in mediating higher-order oligomerization (Frost et al., 2007). The hypothesis that members of the BAR domain superfamily can form higher-order oligomers on the membrane surface was first suggested by electron micrographs of tubules formed by amphiphysin BAR domains with an arrangement of thin rings, arcs or spirals around their circumference (Takei et al, 1999). Subsequently, bi-functional chemical cross-linkers produced large aggregates when applied to similar *in vitro* preparations (Peter et al., 2004). Finally, Shimada *et al.* reported that purified F-BAR domains also induced tubular membranes that appeared to be encased by a tightly-wound thread of protein oligomers which they proposed were strings of F-BARs held together by a unique tip-to-tip contact observed in their crystal structures (Shimada et al, 2007). This is an important line of investigation, as it addresses the overlooked fact individual BARs can only generate local, microscopic membrane curvature, whereas macroscopic transformations—like those observed during endocytosis of coat-pits or elongation of tubular carriers between organelles—require the ensemble effort of many proteins acting in close proximity. In light

of this, it is usually assumed that biologically meaningful membrane deformations require the formation of protein coats to shape or stabilize the underlying membrane, presumably through direct interactions between individual protomers. However, theoretical considerations have suggested the possibility that even in the absence of protein-protein interactions, protein-induced changes in bilayer properties may create attractive forces that cause microscopically bent bilayer regions to coalesce into macroscopic curvature domains (Ayton et al., 2007; Bruinsma and Pincus, 1996; Reynwar et al., 2007).

Context and Significance of the Current Investigation

Until now, there had been no direct evidence for the shape-based "scaffolding" hypothesis, other than that purified domains generate tubules *in vitro* whose curvature correlates with the concavity of their quaternary structure: classical BARs generate narrower tubules than elongated and gently-curved F-BARs (Farsad et al., 2001; Henne et al., 2007; Itoh et al., 2005; Peter et al., 2004; Shimada et al., 2007; Takei et al., 1999). Conversely, I-BAR modules appear to generate filopodia *in vitro* and in living cells (tubules of the opposite curvature) by binding to the plasma membrane via a convex surface (Mattila et al., 2007). There is stronger evidence that some members of the BAR domain superfamily employ the second mechanism of protein-induced "buckling" through insertion of amphipathic sequences (Zimmerberg and Kozlov, 2006). Like epsin-family proteins (Ford et al., 2002), biochemical (Farsad et al., 2001; Henne et al., 2007) and spectroscopic (Gallop et al., 2006) data suggest that the eponymous N-terminal helix of endophilin and amphiphysin do act like "wedges" that penetrate into one bilayer leaflet. However, no such wedge sequences have been identified within or flanking any of the known F-BAR domains. Finally, whether

members of the BAR domain superfamily in general, or F-BAR modules in particular, form supra-molecular protein coats has been a matter of speculation. While direct protomer interactions enable the polymerization of spherical or cylindrical coats for proteins like clathrin and its adaptors (Brett and Traub, 2006) and the GTPase dynamin (Hinshaw and Schmid, 1995; Takei et al., 1995; Zhang and Hinshaw, 2001), the inherent curvature of individual BAR modules may obviate the need for coat formation.

In short, scaffolding, amphipathic wedges, and collective coat formation may each contribute to curvature generation and stabilization by members of the BAR domain superfamily, but testing these hypotheses directly requires molecular-scale visualization of the proteins in their membrane-bound contexts. The experiments performed here accomplish this goal, and clearly shown that tubule formation by select F-BAR domains results through a shape-based scaffolding mechanism that is amplified by the self-assembly of a helical coat, with no apparent contribution from the insertion of amphipathic sequences.

References

Aspenstrom, P. (1997). A Cdc42 target protein with homology to the non-kinase domain of FER has a potential role in regulating the actin cytoskeleton. Current Biology *7*, 479-487.

Ayton, G. S., Blood, P. D., and Voth, G. A. (2007). Membrane remodeling from N-BAR domain interactions: insights from multi-scale simulation. Biophys J *92*, 3595-3602.

Brett, T. J., and Traub, L. M. (2006). Molecular structures of coat and coat-associated proteins: function follows form. Curr Opin Cell Biol *18*, 395-406.

Bruinsma, R., and Pincus, P. (1996). Protein aggregation in membranes. Current Opinion in Solid State & Materials Science *1*, 401-406.

Casal, E., Federici, L., Zhang, W., Fernandez-Recio, J., Priego, E. M., Miguel, R. N., DuHadaway, J. B., Prendergast, G. C., Luisi, B. F., and Laue, E. D. (2006). The crystal structure of the BAR domain from human Bin1/amphiphysin II and its implications for molecular recognition. Biochemistry *45*, 12917-12928.

Chitu, V., and Stanley, E. R. (2007). Pombe Cdc15 homology (PCH) proteins: coordinators of membrane-cytoskeletal interactions. Trends in Cell Biology *17*, 145-156.

Chothia, C., Levitt, M., and Richardson, D. (1981). Helix to helix packing in proteins. J Mol Biol *145*, 215-250.

Farsad, K., Ringstad, N., Takei, K., Floyd, S. R., Rose, K., and De Camilli, P. (2001). Generation of high curvature membranes mediated by direct endophilin bilayer interactions. J Cell Biol *155*, 193-200.

Ford, M. G., Mills, I. G., Peter, B. J., Vallis, Y., Praefcke, G. J., Evans, P. R., and McMahon, H. T. (2002). Curvature of clathrin-coated pits driven by epsin. Nature *419*, 361-366.

Frost, A., De Camilli, P., and Unger, V. M. (2007). F-BAR Proteins Join the BAR Family Fold. Structure *15*, 751-753.

Gallop, J. L., Jao, C. C., Kent, H. M., Butler, P. J., Evans, P. R., Langen, R., and McMahon, H. T. (2006). Mechanism of endophilin N-BAR domain-mediated membrane curvature. Embo J *25*, 2898-2910.

Habermann, B. (2004). The BAR-domain family of proteins: a case of bending and binding? EMBO Rep *5*, 250-255.

Henne, W. M., Kent, H. M., Ford, M. G. J., Hegde, B. G., Daumke, O., Butler, P. J. G., Mittal, R., Langen, R., Evans, P. R., and McMahon, H. T. (2007). Structure and Analysis of FCHo2 F-BAR Domain: A Dimerizing and Membrane Recruitment Module that Effects Membrane Curvature. Structure *15*, 1-14.

Hinshaw, J. E., and Schmid, S. L. (1995). Dynamin self-assembles into rings suggesting a mechanism for coated vesicle budding. Nature *374*, 190-192.

Itoh, T., and De Camilli, P. (2006). BAR, F-BAR (EFC) and ENTH/ANTH domains in the regulation of membrane-cytosol interfaces and membrane curvature. Biochim Biophys Acta *1761*, 897-912.

Itoh, T., Erdmann, K., Roux, A., Habermann, B., Werner, H., and De Camilli, P. (2005). Dynamin and the actin cytoskeleton cooperatively regulate plasma membrane invagination by BAR and F-BAR proteins. Dev Cell *9*, 791–804.

Kamioka, Y., Fukuhara, S., Sawa, H., Nagashima, K., Masuda, M., Matsuda, M., and Mochizuki, N. (2004). A novel dynamin-associating molecule, formin-binding protein 17, induces tubular membrane invaginations and participates in endocytosis. J Biol Chem *279*, 40091-40099.

Kumar, S., and Bansal, M. (1996). Structural and sequence characteristics of long alpha helices in globular proteins. Biophys J *71*, 1574-1586.

Lassmann, T., and Sonnhammer, E. L. (2005). Kalign--an accurate and fast multiple sequence alignment algorithm. BMC Bioinformatics *6*, 298.

Lassmann, T., and Sonnhammer, E. L. (2006). Kalign, Kalignvu and Mumsa: web servers for multiple sequence alignment. Nucleic Acids Res *34*, W596-599.

Lee, E., Marcucci, M., Daniell, L., Pypaert, M., Weisz, O. A., Ochoa, G. C., Farsad, K., Wenk, M. R., and De Camilli, P. (2002). Amphiphysin 2 (Bin1) and T-tubule biogenesis in muscle. Science *297*, 1193-1196.

Lee, S., Kerff, F., Chereau, D., Ferron, F., Klug, A., and Dominguez, R. (2007). Structural Basis for the Actin-Binding Function of Missing-in-Metastasis. Structure *15*, 145-155.

Li, J., Mao, X., Dong, L. Q., Liu, F., and Tong, L. (2007). Crystal Structures of the BAR-PH and PTB Domains of Human APPL1. Structure *15*, 525-533.

Lippincott, J., and Li, R. (2000). Involvement of PCH family proteins in cytokinesis and actin distribution. Microscopy Research and Technique *49*, 168-172.

Masuda, M., Takeda, S., Sone, M., Ohki, T., Mori, H., Kamioka, Y., and Mochizuki, N. (2006). Endophilin BAR domain drives membrane curvature by two newly identified structure-based mechanisms. Embo J *25*, 2889-2897.

Mattila, P. K., Pykalainen, A., Saarikangas, J., Paavilainen, V. O., Vihinen, H., Jokitalo, E., and Lappalainen, P. (2007). Missing-in-metastasis and IRSp53 deform PI(4,5)P2-rich membranes by an inverse BAR domain-like mechanism

10.1083/jcb.200609176. J Cell Biol *176*, 953-964.

Millard, T. H., Bompard, G., Heung, M. Y., Daffom, T. R., Scott, D. J., Machesky, L. M., and Futterer, K. (2005). Structural basis of filopodia formation induced by the IRSp53/MIM homology domain of human IRSp53. Embo J *24*, 240-250.

Parry, D. A., Dixon, T. W., and Cohen, C. (1992). Analysis of the three-alpha-helix motif in the spectrin superfamily of proteins. Biophys J *61*, 858-867.

Peter, B. J., Kent, H. M., Mills, I. G., Vallis, Y., Butler, P. J., Evans, P. R., and McMahon, H. T. (2004). BAR domains as sensors of membrane curvature: the amphiphysin BAR structure. Science *303*, 495-499.

Pylypenko, O., Lundmark, R., Rasmuson, E., Carlsson, S., and Rak, A. (2007). The PX-BAR membrane-remodeling unit of sorting nexin 9. The EMBO Journal.

Reynwar, B. J., Illya, G., Harmandaris, V. A., Muller, M. M., Kremer, K., and Deserno, M. (2007). Aggregation and vesiculation of membrane proteins by curvature-mediated interactions. Nature *447*, 461-464.

Shimada, A., Niwa, H., Tsujita, K., Suetsugu, S., Nitta, K., Hanawa-Suetsugu, K., Akasaka, R., Nishino, Y., Toyama, M., Chen, L., *et al.* (2007). Curved EFC/F-BAR-Domain Dimers Are Joined End to End into a Filament for Membrane Invagination in Endocytosis. Cell *129*, 761-772.

Suetsugu, S., Murayama, K., Sakamoto, A., Hanawa-Suetsugu, K., Seto, A., Oikawa, T., Mishima, C., Shirouzu, M., Takenawa, T., and Yokoyama, S. (2006). The RAC Binding Domain/IRSp53-MIM Homology Domain of IRSp53 Induces RAC-dependent Membrane Deformation

10.1074/jbc.M606814200. J Biol Chem *281*, 35347-35358.

Takei, K., McPherson, P. S., Schmid, S. L., and De Camilli, P. (1995). Tubular membrane invaginations coated by dynamin rings are induced by GTP-gamma S in nerve terminals. Nature *374*, 186-190.

Takei, K., Slepnev, V. I., Haucke, V., and De Camilli, P. (1999). Functional partnership between amphiphysin and dynamin in clathrin-mediated endocytosis. Nat Cell Biol *1*, 33-39.

Tarricone, C., Xiao, B., Justin, N., Walker, P. A., Rittinger, K., Gamblin, S. J., and Smerdon, S. J. (2001). The structural basis of Arfaptin-mediated cross-talk between Rac and Arf signalling pathways. *411*, 215-219.

Tsujita, K., Suetsugu, S., Sasaki, N., Furutani, M., Oikawa, T., and Takenawa, T. (2006). Coordination between the actin cytoskeleton and membrane deformation by a novel membrane tubulation domain of PCH proteins is involved in endocytosis

10.1083/jcb.200508091. J Cell Biol *172*, 269-279.

Weissenhorn, W. (2005). Crystal structure of the endophilin-A1 BAR domain. J Mol Biol *351*, 653-661.

Zhang, P., and Hinshaw, J. E. (2001). Three-dimensional reconstruction of dynamin in the constricted state. Nat Cell Biol *3*, 922-926.

Zhu, G., Chen, J., Liu, J., Brunzelle, J. S., Huang, B., Wakeham, N., Terzyan, S., Li, X., Rao, Z., Li, G., and Zhang, X. C. (2007). Structure of the APPL1 BAR-PH domain and characterization of its interaction with Rab5. Embo J.

Zimmerberg, J., and Kozlov, M. M. (2006). How proteins produce cellular membrane curvature. Nat Rev Mol Cell Biol *7*, 9-19.

Chapter 2: Structural Basis of Membrane Invagination by F-BAR Domains

Using a structural approach that allows for the presence of a membrane holds the potential to advance a mechanistic description of membrane remodeling by answering four immediate questions: first, it would visualize directly how members of the BAR superfamily interact with the bilayer. Second, it would provide insight into the ensemble component of protein-induced membrane curvature. Third, it would explain whether and how the same type of domain accommodates a spectrum of different membrane curvatures. Fourth, structures may suggest how spatial regulation of membrane deformation is achieved. By showing directly how F-BARs employ a combination of scaffolding and ensemble action to induce curvature, this study provides answers to these questions.

F-BAR PROTEINS SPONTANEOUSLY SEGREGATE FROM CLASSICAL BAR PROTEINS DURING MEMBRANE TUBULE FORMATION

High-level expression of fluorescently-labeled F-BAR proteins revealed that they generate membrane tubules inside living cells (Itoh et al., 2005; Tsujita et al., 2006). Less appreciated but presumably of functional significance, F-BAR and other BAR superfamily proteins physically segregated from each other on membrane surfaces during membrane remodeling as seen in Fig. 2-1A (Itoh and De Camilli, 2006). While segregation is likely to be determined in part by the affinity of a given BAR superfamily domain for a specific degree of curvature, the dynamic alternation of F-BAR and N-BAR microdomains (Fig. 2-1A)

Fig. 2-1: F-BAR versus N-BAR Tubulation in Living Cells: Spontaneous Segregation, Differences in Diameter and Rigidity.

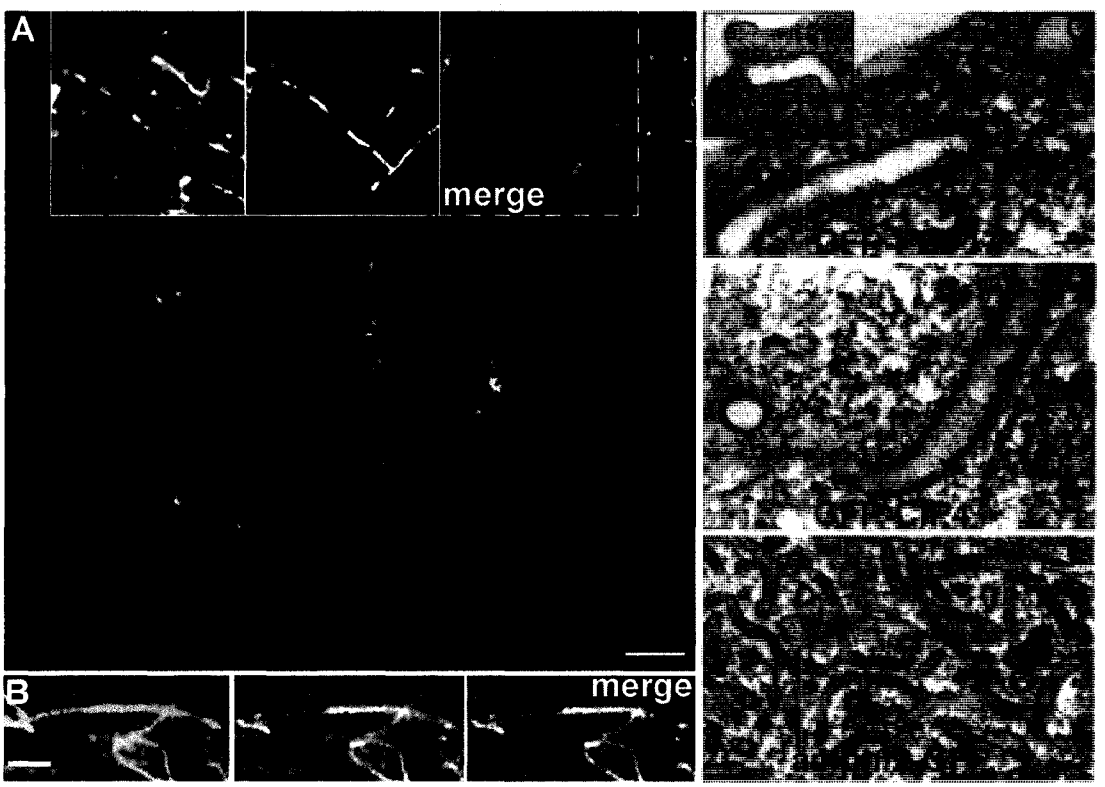

A) COS7 cell simultaneously transfected with amphiphysin2-GFP (green) and RFP-FBP17 (red) produces tubular networks in which the two proteins segregate from each other. Insets show the GFP, RFP, and merged channels. B) High magnification image of a cell transfected with GFP-CIP4 (left) and mRFP-FBP17 (middle) demonstrating the absence of segregation between the two proteins (merge; right). C) large invaginations of the plasma membrane observed by electron microscopy of thin-sections from COS7 cells transfected with full-length human GFP-FBP17 and D) GFP-CIP4; in comparison with the smaller tubules formed by amphiphysin2-GFP (E). Bars (A) 1 μm, (B) 0.5 μm, (C-E) 70 nm.

suggested that stereotyped protein-protein interactions enabled members of the BAR superfamily to distinguish and recruit self-similar domains during membrane remodeling. In support of this hypothesis, when two different F-BAR proteins from the Toca family (transducer of Cdc42-dependent actin assembly (Ho et al., 2004)), namely CIP4/Toca-3 and FBP17/Toca-2, were co-expressed they co-localized on the same tubules (Fig. 2-1B). While interactions between highly homologous TOCA proteins may involve more than a single domain, it is most likely that co-localization of these proteins was driven by their highly conserved and structural homologous membrane-binding F-BAR domains (Shimada et al., 2007).

F-BAR TUBULES ARE LARGER THAN N-BAR TUBULES IN LIVING CELLS

When analyzed in living cells, F-BAR tubules were >3-fold wider in diameter than tubules formed by N-BARs, as shown by thin-section electron microscopy of COS7 cells expressing GFP-FBP17 (Fig. 2-1C and inset), GFP-CIP4 (Fig. 2-1D) and GFP-amphiphysin-2 (Fig. 2-1E). This observation mirrors data that were previously obtained *in vitro* (Henne et al., 2007; Itoh et al., 2005; Shimada et al., 2007; Tsujita et al., 2006), emphasizing that tubulation *in vitro* generates biologically relevant structures. In addition, the striking differences in tubule diameters supported the scaffolding hypothesis, as the size difference between F-BAR and N-BAR tubules in living cells correlated directly with the difference in the radii of curvature for the respective domains (Casal et al., 2006; Shimada et al., 2007).

Fig. 2-2: Reconstitution of CIP4 F-BAR Induced Tubulation and Segregation from Endophilin N-BAR Domains *in vitro*.

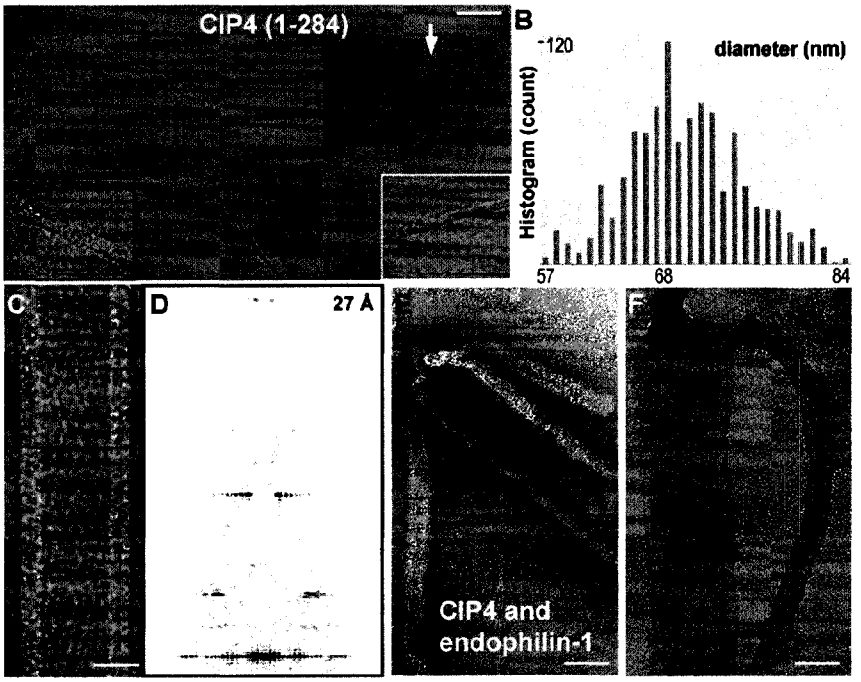

A) electron (cryo)micrograph of a nascent tubule generated *in vitro* by F-BAR domains (human CIP4, 1-284). The yellow arrow points to the demarcation between the membrane surface with and without F-BARs, revealing a smooth bilayer to the right and adsorbed protein to the left, as seen in the 2x enlarged inset surrounded by the yellow box. To the left of the yellow arrow, the curvature of the membrane has changed little, if at all, despite the presence of bound proteins. Induction of tubule formation accompanies self-organization of F-BAR domains into a helical coat (cyan arrow and enlarged inset). B) Histogram of tubule widths generated *in vitro*. C) electron (cryo)micrograph of a tubule following temperature annealing and its corresponding Fourier Transform (D), which displays layerlines beyond ~27 Å. E,F) Liposomes co-incubated with F-BAR (CIP4) and N-BAR (endophilin-1) proteins *in vitro* observed after negative staining with uranyl formate (E) or uranyl acetate (F), displaying contiguous membrane tubules whose change in diameter corresponds with the change in the radius of curvature for F-BAR versus N-BAR domains. Bars (A) 300 Å; (C) 25 nm; (E,F) 40 nm.

IN VITRO RECONSTITUTION OF MEMBRANE TUBULATION BY F-BAR DOMAINS FOR STRUCTURAL ANALYSIS BY ELECTRON CRYO-MICROSCOPY

To structurally analyze F-BAR induced membrane deformation, we generated mixed populations of tubules *in vitro* whose range of diameters were consistent with the range observed in living cells (57-85 nm *in vitro* compared with 64-113 nm in living cells, Fig. 2-2A,B). Notably, micrographs of unstained liposomes caught in the process of tubule formation illustrated that tubulation involved at least two intermediate steps that correlated with the re-organization F-BAR domains into a defined coat following their adsorption onto the membrane. In Fig. 2-2A, a bare bilayer is clearly resolved to the right of the yellow arrow and more clearly in the 2X enlarged inset. Immediately to the left of the yellow arrow, the outer surface of the bilayer is decorated by bound F-BAR domains but the curvature of the membrane has changed little if at all, in comparison with the naked membrane to the right. Between the yellow and cyan arrows, the F-BAR domains have clearly self-organized into a structured coat, and it is the organization of the coat that appears to transform the spherical liposome into a cylindrical tubule. Under the same solution conditions, when an N-BAR domain protein was mixed with an F-BAR domain protein *prior* to incubation with liposomes, homogeneous microdomains with a constant diameter—corresponding with the curvature of the F-BAR domain—were contiguous with equally homogenous but distinct tubules whose smaller diameter corresponded with the curvature of the N-BAR domain (Fig. 2-2E,F). These *in vitro* observations were in accord with segregation observed in living cells.

The heterogeneity within populations of tubules, subtle changes in diameter along individual tubules, and the loss of lattice coherence over long distances presented significant obstacles to 3D reconstruction. Fortuitously, the long range order of the CIP4 F-BAR coat could be improved by subjecting F-BAR tubules to a period of slow temperature annealing

before vitrification (see methods). In electron (cryo)micrographs of annealed tubules the helical nature of the F-BAR coat was obvious (Fig. 2-2C) and Fourier transforms of these images revealed strong layer-lines (Fig. 2-2D). Temperature annealing was only used to generate images suitable for structure determination. All other *in vitro* tubulation reactions were performed at room temperature for up to 30 minutes.

ITERATIVE HELICAL REAL SPACE RECONSTRUCTION OF F-BAR TUBULES

We employed the Iterative Helical Real Space Reconstruction algorithm (Egelman, 2000) to reconstruct volumes from individual tubules composed of up to ~3000 F-BAR domains, after preliminary efforts with Fourier-Bessel reconstruction failed to achieve the desired resolution (Figs. 2-4, see also Appendix II, Figs. AII-3 & AII-4). This approach enabled us to resolve individual F-BAR dimers and the contacts defining the helical coat (Fig. 2-3). To our knowledge, this is the first reconstruction of a membrane-binding protein with sufficient resolution to unambiguously identify individual protein subunits adsorbed onto an underlying membrane. The membrane itself appeared relatively smooth, with a hydrophobic core that was ~26Å thick and phosphocholine headgroup regions that were ~12Å thick (Fig. 2-3C). The correspondence between the dimensions of the bilayer in our reconstructions and measurements of similar synthetic lipid mixtures strongly supported the validity of these results (Rodriguez et al., 2007; Wang et al., 2006). Notably, in reconstructions calculated from images of tubules with broken-open ends (Fig. AII-3), there was additional unstructured density along the surface of the inner leaflet. Since 3D reconstruction depends on averaging, we cannot rule out entirely that randomly distributed lipid protrusions were responsible for this layer of unstructured density. However, since this additional layer was observed only in tubes that were broken open, and given that the F-

BAR domain was the only protein added to the reaction mixture, it seemed more likely that the additional densities represented a disordered layer of protein. This observation was significant because it, unexpectedly, conveyed that F-BARs could apparently bind to membranes with convex curvature. Mechanistically, this reinforced the idea that membrane-binding and membrane-bending are separable events (Fig. 2-2A).

Fig. 2-3: Single Particle Helical Reconstruction of an F-BAR Induced Tubule.

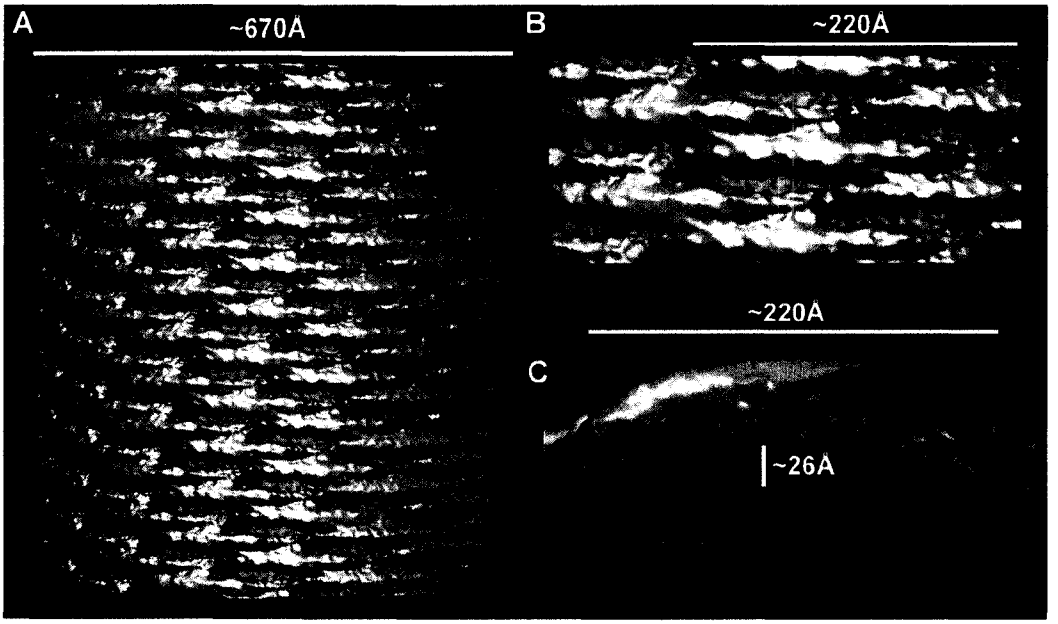

A) Surface of a ~67 nm diameter membrane tubule at ~ 17 Å resolutions. The protein coat is colored blue-gray and the underlying membrane is green. B) Zoom in on the lattice seen orthogonal to the cylindrical axis, highlighting the tip-to-tip interactions and the broad contacts between laterally-adjacent dimers. C) Cross-sectional slab through one dimer parallel with the plane of the tip-to-tip interaction. There are four clearly resolved points of membrane binding. The hydrophobic core of the phospholipid bilayer is ~26 Å thick and the headgroup regions are ~12Å thick.

Fig. 2-4: Experimental versus Model 2D Fourier Transforms.

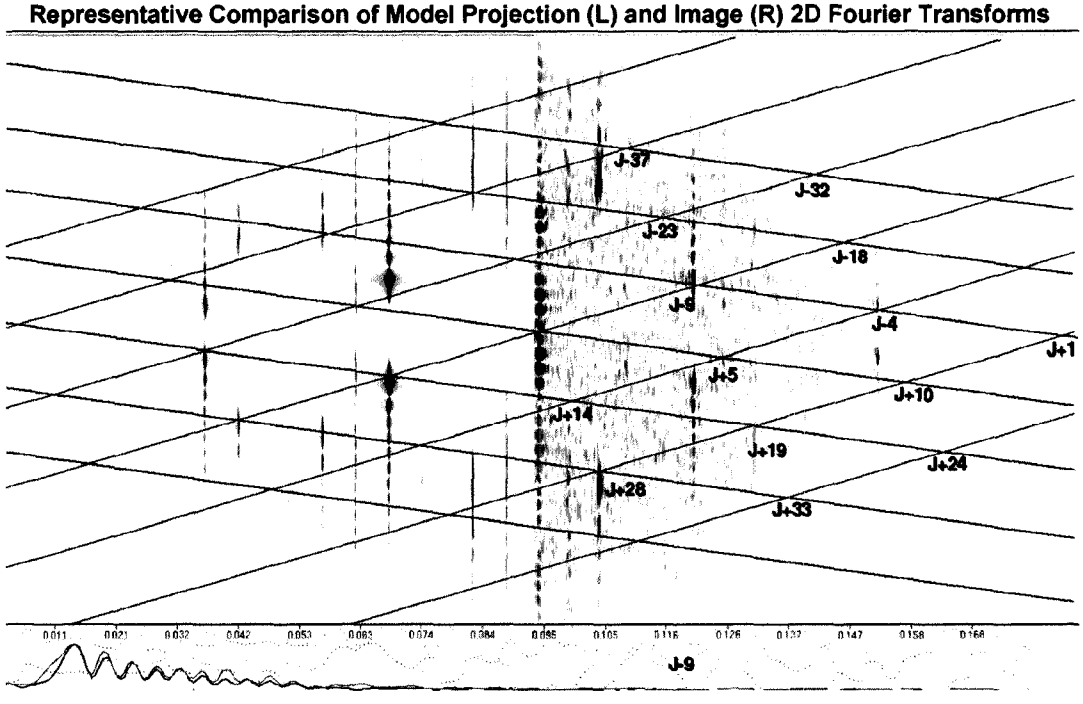

Right: Fourier transform of the aligned, straightened tubule overlaid with the lattice and annotated with the Bessel function orders used for a preliminary Fourier-Bessel reconstruction. Left: Fourier transform of a 2D projection image calculated from a helical reconstruction, overlaid with the same lattice. Bottom: Amplitude (continuous) and Phase (dotted) modulation of pixels values along the layerline corresponding with the J-9 Bessel function from the experimental (right) image data. The phase modulations for the near and far sides of the function are precisely 180° out of phase with each other, consistent with the assignment of an odd Bessel order. Analysis performed with SUPRIM and PHOELIX (Schroeter and Bretaudiere, 1996; Whittaker et al., 1995).

DIRECT VISUALIZATION OF SCAFFOLDING BY F-BAR DOMAINS

Like other BAR superfamily domains, F-BAR tubulation requires the presence of anionic headgroups to be present in the membrane at >10 mol% (Itoh et al., 2005; Tsujita et al., 2006). Moreover, tubulation was inhibited by increasing solution ionic strength, such that tubule formation was blocked at >300mM [NaCl] (data not shown), demonstrating that membrane deformation by F-BARs depended on electrostatic interactions. Consistent with these observations, the scaffolding hypothesis predicts that defined points of contact between the protein's clusters of cationic residues and the phospholipid headgroups constrain the membrane to match the curvature of the domain. Proving this model, the 3D reconstruction visualized how through four points of close apposition the F-BAR dimer imposed its own shape on the underlying bilayer (Fig. 2-3C, 2-5B). Moreover, there was no significant difference between the curvature of the F-BAR dimer bound to tubules and the structure obtained from x-ray crystallography in the absence of lipids (Fig. 2-5B). This observation established the additional feature of the scaffolding hypothesis positing that protein scaffolds must be more rigid than the membrane.

To identify which residues participated in membrane binding at these four sites, the atomic coordinates of the F-BAR domains of human FBP17 and CIP4 were fit into the map manually and then refined using algorithms implemented in UCSF Chimera (Pettersen et al., 2004) or the program SITUS (Pettersen et al., 2004; Wriggers et al., 1999) with equivalent results. The agreement for the fit of both structures was not surprising given that their crystal structures superimposed to within 2.15Å rmsd between corresponding Cα-atoms (Shimada et al., 2007) (see also Fig. 2-7). As illustrated in Fig. 2-5, two regions of membrane binding near the center of the module appeared to correspond with the cationic clusters composed of R/K27, K30, K33, K110, R113, K114, and R/K150 (where R/K indicates the

Fig. 2-5: Fitting F-BAR Crystal Structures into the CryoEM Map Reveals Membrane-Binding Residues and Possible Lattice Contacts.

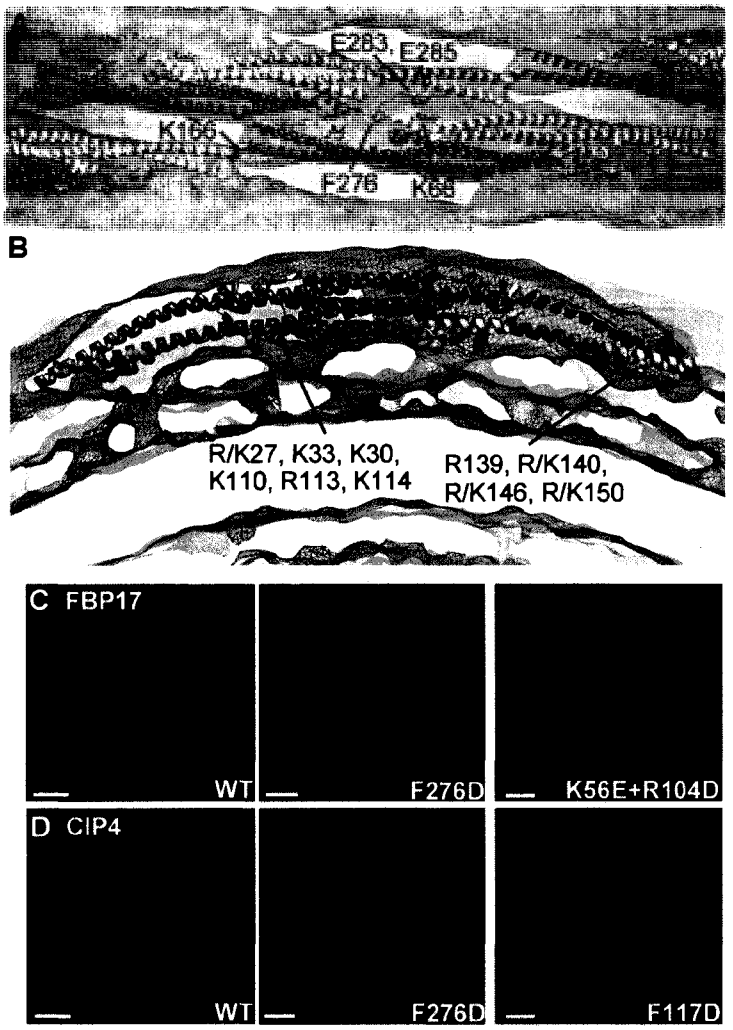

A) Surface representation of a membrane tubule perpendicular to the cylindrical axis, focused on the interactions between four neighboring F-BAR molecules. The underlying membrane is colored in grey and the protein coat in grey mesh. One monomer of each F-BAR module is in yellow, the other in orange-red. Conserved residues hypothesized to contribute to the tip-to-tip and lateral interactions are annotated and shown with space-filling atoms. B) Cross-sectional slab through one dimer parallel with the plane of the tip-to-tip interactions. The four resolved points of membrane binding correspond with clusters of conserved, cationic residues found along the concave faces of both dimers, where R/K indicates the amino acid found in CIP4 or FBP17, respectively (Shimada et al., 2007). C) Representative images of COS7 cells with high levels of expression of wild type or mutated constructs of GFP-FBP17 or D) GFP-CIP4. Some mutations completely abolish membrane localization, while others only compromise tubule formation. Bars 10 μm.

amino acid found in CIP4 or FBP17, respectively). Two additional areas of contact nearer the dimer's tips appeared to correspond with a cluster of cationic residues composed of R139, R/K140, R/K146 and R/K150. Consistent with this interpretation of our map, mutating residues that line the concave face, including K33E, K33Q, R113Q and K114Q, compromise membrane binding and tubule formation (Shimada et al., 2007; Tsujita et al., 2006).

Importantly, there was no evidence at this resolution that extended amphipathic sequences were partially intercalated into the bilayer—distinguishing F-BAR mediated tubulation from the combination of scaffolding plus amphipathic "wedges" employed by N-BAR domains (Farsad et al., 2001; Gallop et al., 2006). However, it is possible, given the moderate resolution of this analysis, that isolated residues shallowly inserted into the outer leaflet of the bilayer. To explore this possibility, we noted from the fit of the atomic coordinates into our reconstruction that F117 faced the membrane from the concave surface of the domain and that it was surrounded by the hydrophobic alkane moieties of cationic residues that mediated binding to lipid headgroups (Fig. 2-6). To test whether possible insertion of F117 into the bilayer contributed to membrane-binding or tubulation, we mutated F117 to Ala and Asp, respectively. The F117A mutant had no observable defects in membrane tubule formation. Given the smaller volume occupied by the hydrophobic side chain of Ala, this suggested that tubulation did not require insertion of a bulky Phe amongst the acyl chains of the membrane. Further supporting this idea, when F117 was mutated to Trp in a Trp-less variant of the domain, no blue-shift of the fluorescence emission spectrum was detectable (data not shown, (Ladokhin et al., 2000)). In contrast, the F117D mutation in FBP17 F-BAR domains potently inhibited tubulation in every reaction condition tested *in vitro* (Fig. 2-8A), while the corresponding mutation in full-length CIP4 also inhibited

tubulation in living cells (Fig. 2-5D). This observation suggested that the F117D mutant was defective in forming high-affinity interactions with the membrane surface via its concave surface. We speculate that the functional defect arose because the Asp strongly interacted with its neighboring cationic residues, partially neutralizing the surface potential and perhaps preventing conformational extensions of Lys and Arg residues toward the membrane surface. In support of the latter, we noted that the molecular envelope of the dimer was continuous with the bilayer exclusively in the four positions that, based on the fit of the crystal structure, were occupied by cationic clusters.

Fig. 2-6: FBP17 F-BAR Mutant Analysis *in vitro*

A) Lower magnification images of samples generated with wild-type protein versus B) the

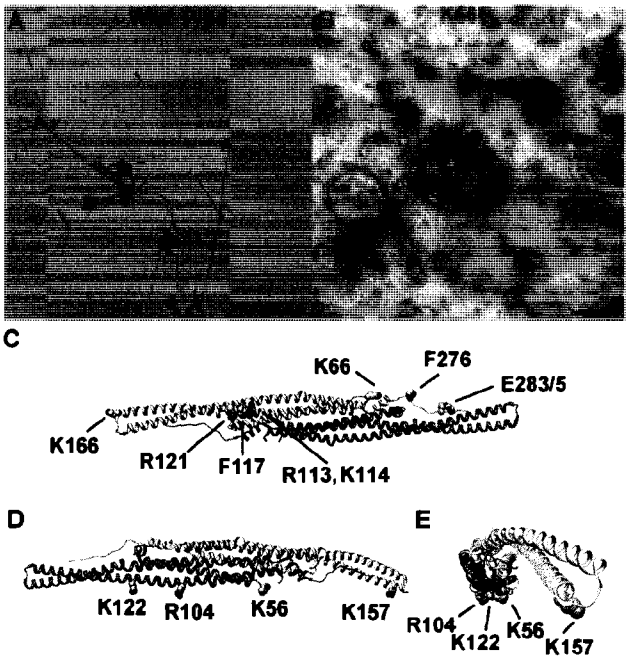

mutant K66E, demonstrating the striking differences in tubule number, length, and rigidity seen *in vitro* and quantified in Fig. 2-8A. C) View of the concave surface of the FBP17 F-BAR domain along the dimer axis with F117 and surrounding residues shown with space-filling atoms. Additional residues mutated in this study are also shown. D) Ribbon diagram of the FBP17 F-BAR domain parallel with the bilayer surface, with the membrane-binding residues that constitute the flat-lattice interface shown with space-filling atoms. E) Same as 'D' but seen along the module's long axis. Bars (C) 2 μm; (D) 500 nm.

F-BAR DOMAINS SELF-ORGANIZE INTO HELICAL LATTICES TO INDUCE TUBULE FORMATION

An important finding of our study was that scaffolding by individual F-BARs was necessary but not sufficient for tubule formation. Specifically, the reconstruction demonstrated that tubule formation involved the collective assembly of F-BARs into a helical coat that propagated curvature around and along the growing tubule. The helical lattice was held together by tip-to-tip and extensive lateral interactions (Fig. 2-3A,B, Fig. 2-5A). Of the two, only the tip-to-tip interaction, mediated in part by K166 in the loop between the α3 and α4 helices, was predicted by the crystal structures (Shimada et al., 2007). Importantly, the 6.3Å translation and 40.3° rotation separating each dimer along the helical path defined by the tip-to-tip interaction did not allow preservation of the reported hydrogen bonding pattern, when the dimer was fit as a rigid body. In fact, attempts to maintain the hydrogen bonding pattern as seen in the crystal structure resulted in a ~50% decrease in the correlation coefficient between our map and the structure.

The possibility that the tip-to-tip interaction was flexible or underwent rearrangement during polymerization of the helical coat was consistent with the existence of an additional, lateral contact between neighboring dimers. This broad overlapping interaction involved 50% of the dimer's lateral surface, including the loop between α2 and α3, segments of the lateral surface of α3 and α5, and the C-terminal extended peptide (Shimada et al., 2007). Notably, the near-atomic model generated by fitting the crystal structures into our reconstruction suggested specific contacts that may have been important for the formation of the lateral interactions. This included ionic interactions between K66 or K273 in one dimer and E285 or D286 in the other, as well as between D161 or N163 in one dimer and R47 or K51 in the other (Figs. 2-5A and 2-7). There also appeared to be

hydrophobic interactions, including one between directly opposing F276 in both dimers (Figs. 2-5A and 2-7). As shown in the bottom panel of Fig. 2-7, these surface exposed residues are among the most highly conserved throughout the evolution of the Toca proteins, and are oriented on the surface of the model such that if they do participate in lateral interactions, neighboring dimers would overlap by ~50% of their length.

Because of the large number of potential pairwise interactions, we did not probe the importance of all these residues for the purpose of this study. Nevertheless, analysis of a total of 14 mutants along the lateral interface (7 each for CIP4 and FBP17 respectively) revealed that most of them affected tubulation behavior to some extent. Shown here are examples illustrating the spectrum of effects that were observed in living cells with full-length CIP4 or FBP17 (Fig. 2-5C,D) and *in vitro* with purified FBP17 F-BAR domains (Fig. 2-8A,B). Considering the large surface area involved in the lateral interaction, we were surprised that some point mutations did compromise tubule formation both *in vitro* and in living cells, at least as potently as the previously reported mutation of the tip-to-tip residue K166 to Ala (Fig. 2-8A and (Shimada et al., 2007). Specifically, replacing F276 with the charged residue Asp in full-length FBP17 and CIP4 potently inhibited tubule formation in living cells (Fig. 2-5C,D). Similarly, the same mutation strongly compromised tubulation *in vitro* using isolated F-BAR domains (Fig. 2-8A). Similarly, reversing the charge of K66 inhibited tubule formation when compared with wild type FBP17 F-BAR domains when assayed under equivalent *in vitro* conditions (Fig. 2-8A, see methods in Appendix II).

Fig. 2-7: Evolutionary Conservation and Comparison of Electrostatic Surface Potentials of F-BARs from CIP4 and FBP17.

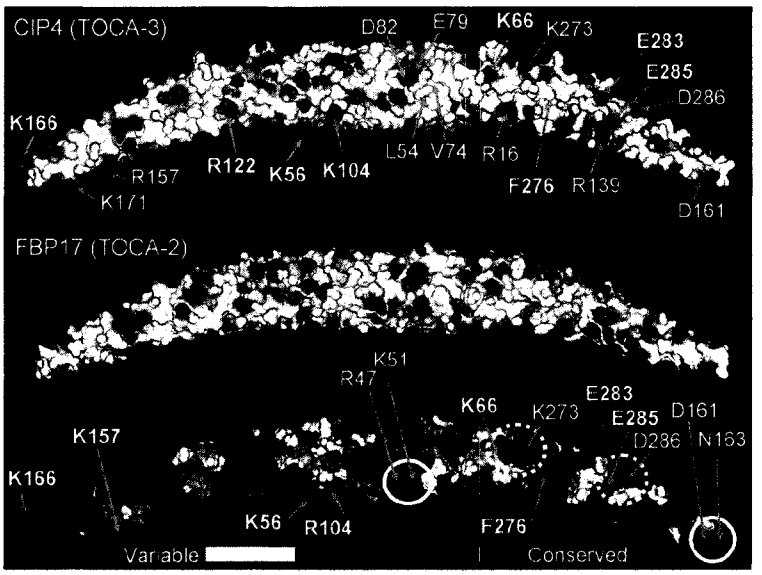

Electrostatic potentials for CIP4 (top) and FBP17 (middle). Residues that may participate in either the lateral overlap (right side) or the 'side-lying' interface (left side) are annotated and the residues mutated in this study are shown in bold type for the CIP4 surface. Conservation of the FBP17 lateral surface, compared with related members of the Toca family, is shown below. Conservation scores were determined from an alignment of residues 1–300 of human FBP17/TOCA-2 (Q96RU3) with sequences of (accession numbers): human CIP4/TOCA-3 (Q15642), human TOCA-1 (Q5T0N5), Chimpanzee (XP_512320), Orangutan (Q5RCJ1), Rat (P97531), Mouse (Q8CJ53), *X. tropicalis* (NP_001072662), zebrafish (Q5U3Q6), *D. melanogaster* (NP_65789), and *C. elegans* (NP_741723). The strongest conservation corresponds with residues that are likely to interact, as predicted by fitting the F-BAR structures into the helical reconstruction. Solid white circles surround anionic residues at the tip of the module that may interact with cationic residues near the center of the module. Dashed white circles surround anionic and cationic residues that are also likely to interact between laterally-overlapping dimers. A conserved hydrophobic patch, including F276, may also contribute to the lateral contacts seen in the helical reconstruction.

Fig. 2-8: Mutant Phenotypes & Tubule Persistence Lengths.

A) Quantification of total tubule number, total tubule length (sum of all tubule lengths measured) as determined from 50 low magnification images evenly sampling one EM grid. B) Quantification of mean tubule diameter from low-magnification images like those in Fig. 2-6A,B. Error bars are the standard deviation for the population of tubules. C) Still images of video-DIC recordings of amphiphysin & FBP17. D) Each data point is the rms^2 (root mean square to the square) of 100 tip-to-base measurements of a tubule as a function of total tubule length. The persistence length (L_p) was determined by fitting the data with a theoretical curve according to the equation: $\delta R^2(t) = 2(L_p)^2[x/L_p - 1 + e^{(-x/L_p)}]$; where $\delta R^2(t)$ is the rms^2, x the total length and L_p the persistence length (Derenyi et al., 2002; Le Goff et al., 2002a; Le Goff et al., 2002b). Bars (A,B) 10 μm (C) 5 μm.

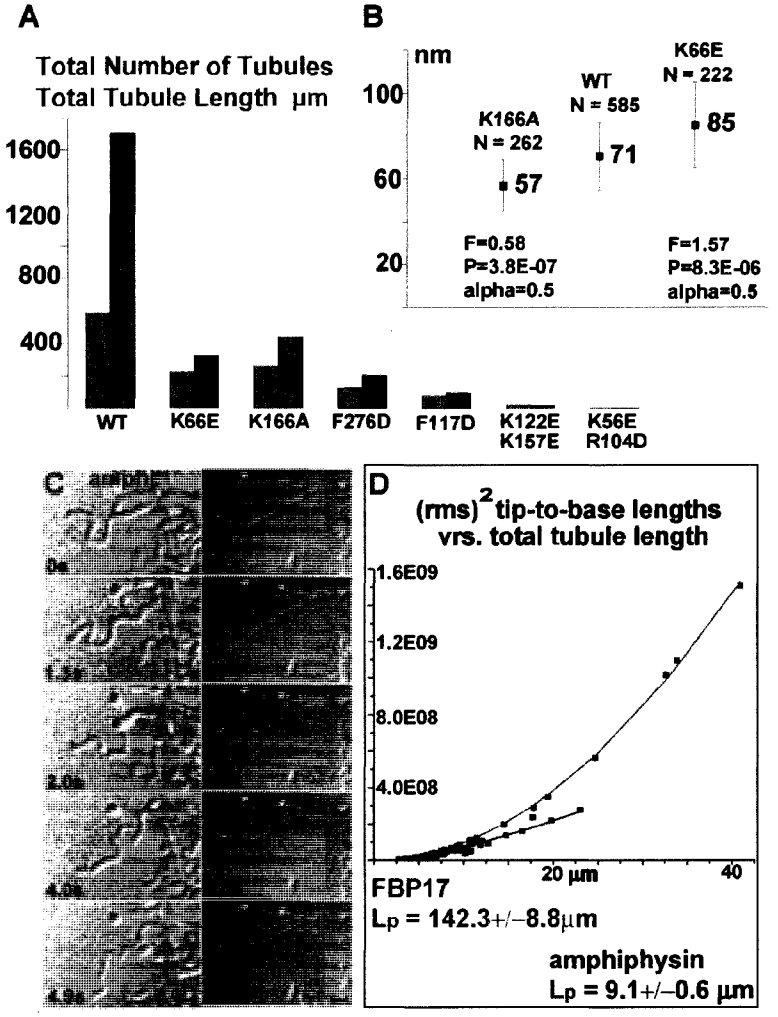

The importance of the lateral interactions was further underscored by electron microscopic examination of the filaments formed in the absence of liposomes by the F-BAR domains of FBP17 or CIP4 (Itoh et al., 2005). Being 12-13 nm thick and with a 4-5 nm repeat distance, they must be composed of both lateral and tip-to-tip interactions (Fig. 2-9), which contrasts with a previous proposal that the length of the F-BAR dimer corresponds to one periodic repeat of these filaments (Shimada et al., 2007).

Figure 2-9: Isolated F-BAR Domains Polymerize into Filaments Composed of Lateral and Tip-to-Tip Interactions in the Absence of Lipids.

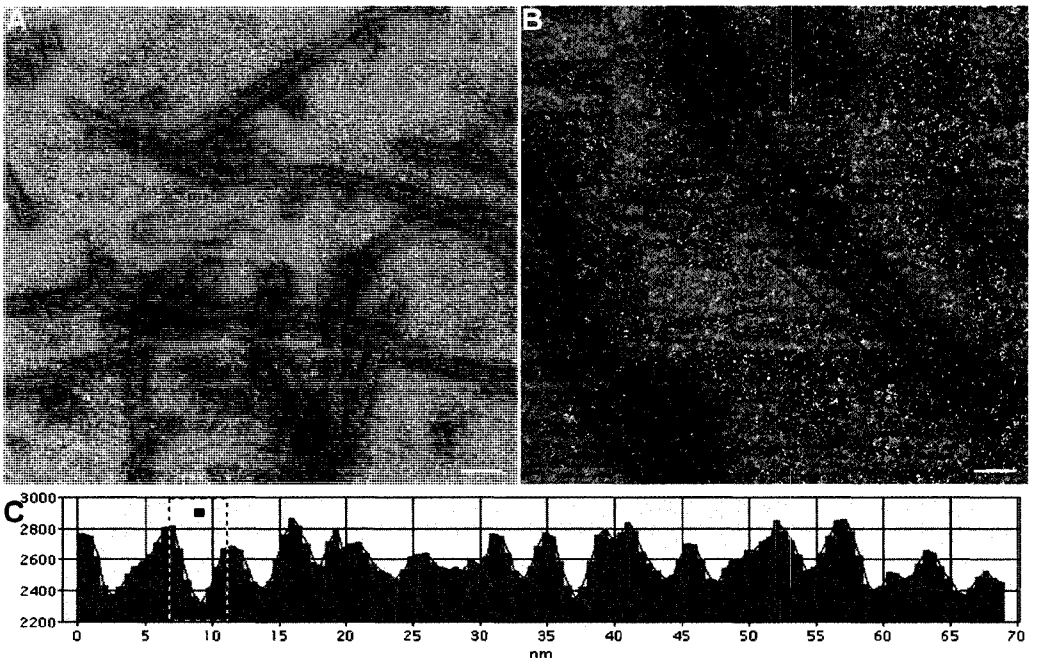

A) Low and B) high power views of negatively stained filaments composed of purified F-BAR domains (CIP4 1 – 284aa) in 100mM NaCl buffered solution without lipids or detergents. C) Pixel values sampled along the center of the filament corresponding with the region indicated by the blue line in 'B' revealing a periodicity of 4-5 nm. Bars (A) 46 nm; (B) 12nm.

THE F-BAR COAT IS MORE RIGID THAN N-BAR OR DYNAMIN COATS

The extensive interactions between dimers observed in the reconstruction explained why F-BAR coated tubules seemed to be more rigid than tubules coated by classical BAR domains. To quantify the difference in the rigidities of N-BAR and F-BAR tubules *in vitro*, we calculated their persistence length, L_p, which is a measure of macromolecular rigidity expressed as the length over which correlations in the direction of the tangent are lost. For FBP17-coated tubules, we determined an L_p of 142.3±8.8 μm. In comparison, amphiphysin-coated tubules had an L_p of 9.1±0.6 μm while dynamin-coated tubules, which were used as a non-BAR superfamily control sample, had an L_p of 37.3±4.6 μm (Fig. 2-8C,D; dynamin data not shown). The 16-fold smaller L_p for amphiphysin tubules compared with FBP17 tubules may have been due partly to their thinner diameter, though it would be of interest to determine whether N-BAR dimers form less extensive inter-molecular contacts than those of the F-BAR coat. Similarly, the 4-fold smaller L_p observed for dynamin, which also forms tubular coats, suggested that the contacts making up the dynamin coat were either less constraining than those of the F-BAR coat or, less-likely, that F-BAR dimers were more rigid than dynamin dimers (Chen et al., 2004; Zhang and Hinshaw, 2001).

VARIABILITY IN COAT ARCHITECTURE ALLOWS A RANGE OF TUBULE DIAMETERS TO FORM

F-BAR domains generate different diameter tubules *in vitro* and in living cells (Fig. 2-1C,D; Fig. 2-2B). To determine the structural basis for this variability, we calculated independent reconstructions of tubules with different diameters. These volumes revealed that F-BARs rotated relative to the tubule's cylindrical axis while maintaining their intrinsic curvature (Fig. 2-10). Specifically, tubules with a diameter near the population mean of 67

Fig. 2-10: Independent Reconstructions of Tubules with Different Diameters

A) The narrowest tubule reconstructed is ~56 nm in diameter, with ~8 tip-to-tip dimers around its circumference. Tilting the long axis of the dimer relative to the cylindrical axis

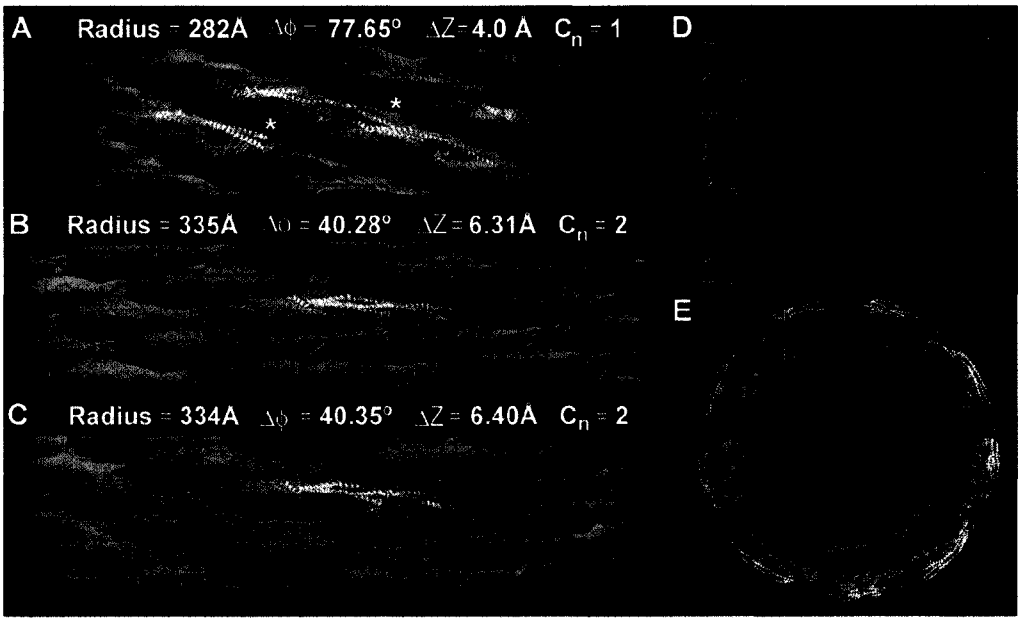

produces a narrower tubule. In this case, the dimers are so steeply tilted that the tip-to-tip contacts appear to be broken (white asterisks). The tubule has no rotational symmetry; the fundamental (J+1) helical symmetry does not describe an inter-molecular contact. Only the near side of the lattice is shown and the underlying membrane has been masked out to emphasize differences in the protein coat. Atomic models of F-BAR domains were fit into the map as rigid bodies. B&C) Two tubules with the same apparent diameter and ~9.5 tip-to-tip dimers around their circumference have resolvable differences in their helical symmetry. D) Central section along the longitudinal axis of the thinnest tubule shown in 'A', demonstrating that the density of the protein coat accommodates rigid atomic models of the F-BAR module that are tilted relative to the cylindrical axis, but whose radius of curvature is unchanged. E) View along the cylindrical axis of the thinner reconstruction shown in 'A' and 'D'.

nm had ~9.5 tip-to-tip dimers around the circumference. In these cases, the long axis of the dimer was only slightly tilted relative to the cylindrical axis, such that a thread of tip-to-tip dimers wrapped around the tubule with a shallow, right-handed twist. Subtle variability in the tilt angle of the dimer still produced resolvable differences in the helical symmetry, and precluded averaging data from different tubules of the same apparent diameter (Fig. 2-10B versus 2-10C). In contrast, the smallest tubule observed was ~57 nm in diameter and accommodated only ~8 dimers around its circumference (Fig. 2-10A). In this case, fitting the dimers into the map suggested that each F-BAR had a left-handed tilt, relative to the cylindrical axis, and the tip-to-tip contacts apparently did not form (Fig. 2-10A, white asterisks).

To test the hypothesis that F-BARs rigidly maintain their intrinsic degree of curvature—even when bound to tubules with smaller diameters—we used the tubule radii and the pitch of the left-handed helical path defined by the lateral interactions to calculate the helical arc length between the center of one dimer and its nearest lateral neighbors. The helical arc lengths for all three tubules—as measured from the reconstructed volumes—were calculated to be 114 +/- 1.5 Å (see Appendix II). This indicates that F-BARs bound to the smaller tubules were not appreciably deformed and that they overlapped their neighbors by the same length, despite being tilted relative to the cylindrical axis (Fig. 2-10A). Moreover, using a complete model of the protein coat, built from 128 copies of the CIP4 F-BAR domain structure, we observed that the density corresponding with the protein coat of the thinnest tubule could be entirely accounted for with rigid but tilted F-BAR modules, interacting via the same lateral contacts (Fig. 2-10D,E). Finally, abolishing the tip-to-tip interaction with the K166A mutation, which produces some tubules *in vitro* but not in living cells (Shimada et al., 2007), appears to bias the population distribution of tubule diameters

toward smaller diameters (Fig. 2-8A,B). This was consistent with the hypothesis that in the absence of the tip-to-tip constraint, F-BAR modules are more likely to tilt relative to the tubule axis and thus produce narrower tubules. In contrast, compromising the formation of the lateral contacts with the K66E mutation biased the population distribution of tubule diameters toward larger diameters (Fig. 2-8B). Taken together, these variations in coat structure, particularly in the angle between the dimer's long axis and the cylindrical axis, emphasized how plasticity in the lattice allows rigid dimers to accommodate a range of curvatures. To our knowledge, this is the first experimental demonstration of this previously predicted corollary of the scaffolding mechanism (Blood and Voth, 2006; Henne et al., 2007).

F-BAR DOMAINS BIND TO FLAT MEMBRANES VIA A SURFACE OTHER THAN THEIR CONCAVE FACE

Raw micrographs of liposomes in the midst of being transformed into tubules by the F-BAR domain displayed regions of the membrane that were clearly decorated by bound protein molecules, but whose curvature had not yet appreciably changed (Fig. 2-2A, enlarged insets). Fortuitously, we were able to observe this intermediate state directly by cooling liposomes below the T_m of the most abundant lipid species used in our experiments (palmitoyl-oleyl-phosphatidylserine), which presumably increased membrane rigidity (Fig. 2-11A,B). Both FBP17 and CIP4 F-BARs bound avidly to these rigid membranes, and formed 2D arrays in which laterally-adjacent dimers aligned in almost perfect register while maintaining tip-to-tip interactions (Fig. 2-11, Fig. 2-12). Unexpectedly and regardless of whether crystals were negatively stained or vitrified, a dozen projection density maps

Fig. 2-11: (Cryo)Electron Micrograph of Co-existing Protein-Filaments, Helical and 2D Lattices; Wide Angle X-Ray Scatter of Lipid Samples; Calculated Fourier Transform, and K66E Mutant Phenotype.

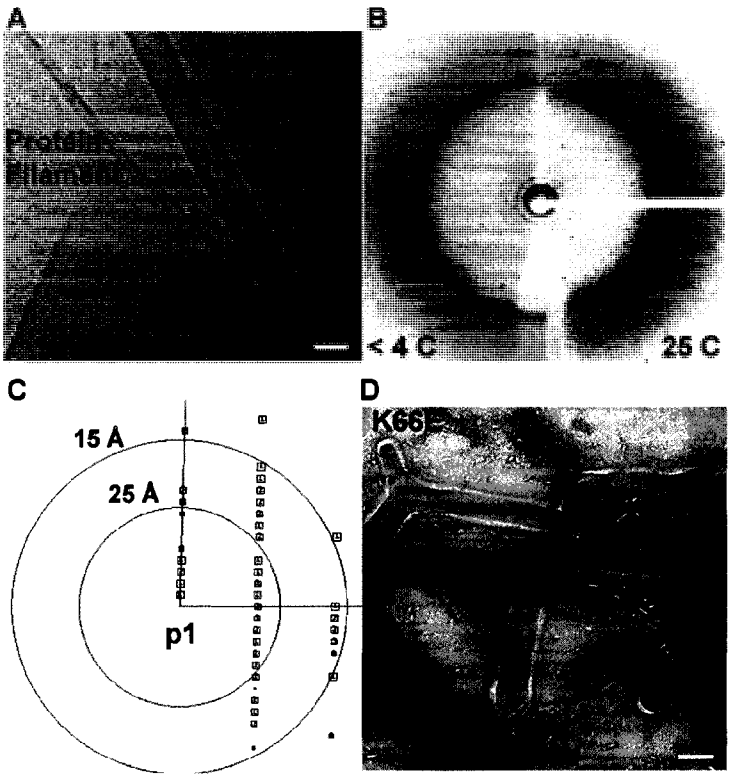

A) Cryo-Electron (micrograph of protein filaments formed by F-BAR domains alongside a 2D lattice and a helical tubule, all formed by the same preparation of human CIP4 residues 1-284. B) Wide-angle X-ray diffractogram of hydrated liposomes equilibrated at 25°C (right side) and <4°C (left side). The synthetic lipid mixture used in this study appears to undergo a temperature-dependent phase transition/separation over this range, at approximately 4°C. The sharp ring at ~4.2Å corresponds with the hexagonal packing of acyl chains. C) Phase error of unique reflections to 15Å calculated for the projection terms of the 3D mtz dataset. The size of the boxes in the plot correspond to the phase error associated with each measurement (1, <8°; 2, <14°; 3, <20°; 4, <30°; 5, <40°; 6, <50°; 7, <80°; 8,<90°, where 90° is random). Box size decreases with increasing phase error. D) Negatively stained sample of the K66E mutant incubated with liposomes at RT, showing a mix of tubules, liposomes, and small strips of the 2D lattices. Bars 70 nm.

calculated from similar but not identical crystals lacked any evidence of the two-fold symmetry that would be observed if the dimers were bound symmetrically to the bilayer via their concave surface (Table 1, Fig. AII-2). The simplest explanation for this absence of a two-fold rotational symmetry was that the domains were bound to the membrane obliquely, such that their maximum curvature surface could not be imposed.

To obtain an estimate for the orientation of the module bound to these rigid membranes, we used a reference library of evenly-spaced projection views of the FBP17 F-BAR domain atomic model (Shimada et al., 2007) to search for the highest correlation with the calculated 2D projection image (Fig. 2-12C). A broad correlation peak was found for views in which the dimer's two-fold axis was rotated by ~60° with respect to the membrane normal. In Fig. 2-12C, ribbon diagrams of the domain in this orientation were superimposed over the projection image, as seen perpendicular to the membrane surface. In Fig. 2-12D, two dimers interacting tip-to-tip are displayed as viewed parallel with the membrane surface (or rotated by 90° with respect to the view in 'C'). In this "side-lying" state, the lateral interactions seen in the helical lattice were unable to form, while the relatively flat membrane-binding surface was composed almost entirely of one monomer (another indication that the intrinsic rigidity of F-BAR dimers exceeds the rigidity of the membrane). A similar side-lying state was recently predicted for N-BAR domains in molecular dynamics simulations, in which a range of curvatures were semi-stable depending on the degree to which the maximum curvature surface was directly imposed on the membrane (Blood and Voth, 2006).

Based on this orientation, our model predicted that the conserved residues K56, K/R104, K122, and K157 played an important role in mediating the electrostatic interaction with the membrane in this 'side-lying state' (Figs. 2-6, 2-7, & 2-12D). Point mutations of any

of these residues to amino acids of the opposite charge abolished 2D lattice formation (Fig. 2-12E), and were observed to have decreased tubulation efficiencies *in vitro* (Fig. 2-6B). Moreover, mutating pairs of them (K122E + K157E or K56E + R104D) potently blocked tubulation *in vitro* with purified F-BAR domains (Fig. 2-8A) and in living cells with full-length GFP-FBP17 (Fig. 2-5C). The K56E + R104D mutation in full-length GFP-FBP17 in living cells was particularly striking, in that it apparently abolished membrane binding entirely and resulted in a diffuse distribution of the associated GFP-signal (Fig. 2-5C).

These observations suggested that F-BAR proteins may form small clusters on membrane surfaces, ready to induce tubule formation (Fig. 2-12F). Importantly, in this side-lying state the lateral interaction surfaces of the F-BAR domain were obscured, which prevented formation of the helical lattice. In support of this idea, the 2D-lattices converted to tubular structures upon warming. The easiest explanation for this behavior would be that the reduced rigidity and membrane-bending energy above the T_m enabled individual dimers to force the bilayer to adopt their intrinsic curvature locally. Consequently, it was this transition to full imposition of the concave face that exposed the module's lateral interaction surfaces to neighboring dimers and allowed the helical coat to polymerize (Fig. 2-12F). This proposed mechanism for tubulation predicted that inhibiting lateral interactions would shift the equilibrium away from tubule generation and towards the formation of 2D arrays. Consistent with this prediction and our model for the lateral contacts (Fig. 2-5A), the mutants K66E and F276D shifted the equilibrium toward the formation of flat lattices even at temperatures $>T_m$ of the principal lipid component (Fig. 2-11D).

Fig. 2-12: F-BAR Modules Can Bind to Flat Membranes via a Surface Other Than Their Concave Face.

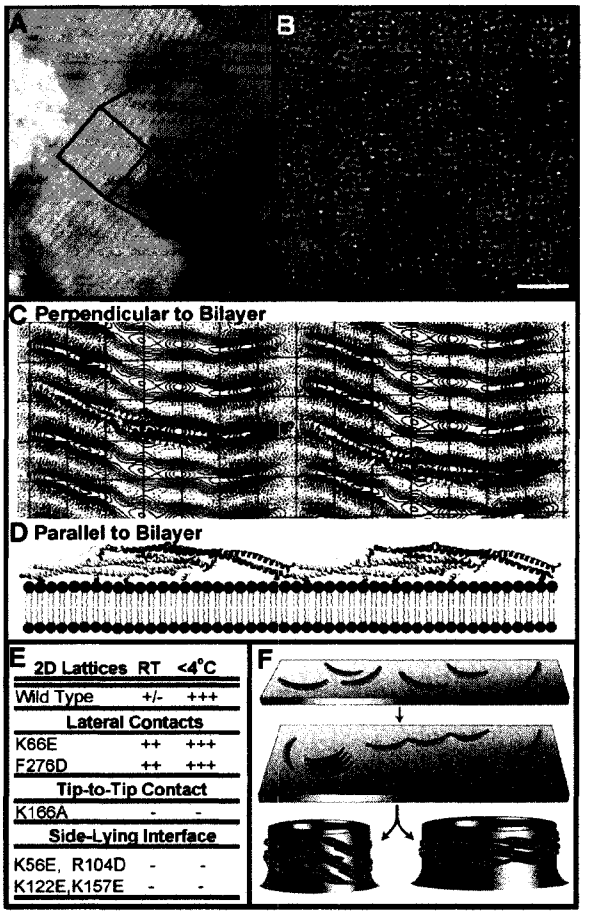

A) Negatively-stained membranes that were pre-cooled before incubation with human FBP17 F-BAR domains. B) Higher magnification of the 2D F-BAR lattice; unit cell a = 33Å b = 214Å γ = 91.0° C) Projection view of the F-BAR domain, calculated from a 3D data set composed of images from a single-axis tilt series over ±40° (representative lattice lines in Fig. AII-2, crystal statistics in Table 1). Ribbon diagrams of the domain are superimposed over the projection image, as seen from the orientation with the highest correlation perpendicular to the membrane surface. D) Two dimers interacting tip-to-tip viewed parallel with the membrane surface, or rotated by 90° with respect to the view in 'C'. Residues likely to mediate membrane-binding in this side-lying state are shown as space-filing atoms from left-to-right: K122, R104, K56, and K157 (see also Figs. 2-6 & 2-7). E) Table of mutant propensity for forming flat lattices at different temperatures. F) Proposed model in which tubule formation proceeds through observable intermediate steps. F-BARs can bind to flat or curved bilayers, clustering in arrays by forming intermolecular interactions. Following the transition to high-affinity binding of the dimer's concave surface, formation of the lateral contacts triggers the vectorial assembly of the helical coat and drives membrane invagination.

TABLE 1 2D CRYSTAL IMAGE STATISTCS

Unit Cell Parameters (n=6)[1]	a = 32.8±0.4 Å b = 213.9±1.0 Å γ = 91.0±0.6°
Images in Single-Axis Tilt Series	13
Tilt Range	±40°
Range of Defocus	1550-3150 Å
Range of Astigmatism	29-600 Å
Number of Observations[2]	304
Number of Fitted Structure Factors	128
Overall weighted phase residual	5.5°

Internal Phase Residual Symmetry Comparisons[3]

		PHASE RESID. COMPAR. vrs. other spots (90° random)		PHASE RESID. SPOTS vrs. Theoretical (45° random)		Target Residuals
1	p1	22.7	66	--	--	
2	p2	59.0	33	29.5	66	37.8
3b	p12_b	58.4	16	36.4	4	27.4
3a	p12_a	57.7	22	41.4	16	30.2
4b	p121_b	59.6	16	33.8	4	27.4
4a	p121_a	52.3	22	25.4	16	30.2
5b	c12_b	58.4	16	36.4	4	27.4
5a	c12_a	57.7	22	41.4	16	30.2
6	p222	61.6	71	29.5	66	31.4
7b	p2221b	61.4	71	31.6	66	31.4
7a	p2221a	63.0	71	34.8	66	31.4
8	p22121	66.0	71	38.4	66	31.4
9	c222	61.6	71	29.5	66	31.4
10	p4	54.3	49	29.9	66	33.9
11	p422	60.6	102	29.5	66	29.7
12	p4212	72.2	102	38.3	66	29.7
13	p3	40.4	20	--	--	25.9
14	p312	49.3	54	28.1	8	26.7
15	p321	58.5	62	39.3	24	28.2
16	p6	61.2	73	29.5	66	31.3
17	p622	63.7	149	37.8	66	28.5

[1] six independent crystals, five imaged after negative staining in 1% uranyl acetate, one imaged under cryo conditions. [2] to 15 Å resolution with $z^* = \pm 0.028$ Å^{-1} [3] Phase residuals were calculated with the program ALLSPACE (Valpuesta et al., 1994). Similar results were obtained for all images of nominally untilted crystals in negative stain and cryo conditions, and for all images obtained within ±10° of tilt.

References

Blood, P. D., and Voth, G. A. (2006). Direct observation of Bin/amphiphysin/Rvs (BAR) domain-induced membrane curvature by means of molecular dynamics simulations. Proc Natl Acad Sci U S A *103*, 15068-15072.

Casal, E., Federici, L., Zhang, W., Fernandez-Recio, J., Priego, E. M., Miguel, R. N., DuHadaway, J. B., Prendergast, G. C., Luisi, B. F., and Laue, E. D. (2006). The crystal structure of the BAR domain from human Bin1/amphiphysin II and its implications for molecular recognition. Biochemistry *45*, 12917-12928.

Chen, Y. J., Zhang, P., Egelman, E. H., and Hinshaw, J. E. (2004). The stalk region of dynamin drives the constriction of dynamin tubes. Nat Struct Mol Biol *11*, 574-575.

Derenyi, I., Julicher, F., and Prost, J. (2002). Formation and interaction of membrane tubes. Phys Rev Lett *88*, 238101.

Egelman, E. (2000). A robust algorithm for the reconstruction of helical filaments using single-particle methods. Ultramicroscopy *85*, 225-234.

Farsad, K., Ringstad, N., Takei, K., Floyd, S. R., Rose, K., and De Camilli, P. (2001). Generation of high curvature membranes mediated by direct endophilin bilayer interactions. J Cell Biol *155*, 193-200.

Gallop, J. L., Jao, C. C., Kent, H. M., Butler, P. J., Evans, P. R., Langen, R., and McMahon, H. T. (2006). Mechanism of endophilin N-BAR domain-mediated membrane curvature. Embo J *25*, 2898-2910.

Henne, W. M., Kent, H. M., Ford, M. G. J., Hegde, B. G., Daumke, O., Butler, P. J. G., Mittal, R., Langen, R., Evans, P. R., and McMahon, H. T. (2007). Structure and Analysis of FCHo2 F-BAR Domain: A Dimerizing and Membrane Recruitment Module that Effects Membrane Curvature. Structure *15*, 1-14.

Ho, H. Y., Rohatgi, R., Lebensohn, A. M., Le, M., Li, J., Gygi, S. P., and Kirschner, M. W. (2004). Toca-1 mediates Cdc42-dependent actin nucleation by activating the N-WASP-WIP complex. Cell *118*, 203-216.

Itoh, T., and De Camilli, P. (2006). BAR, F-BAR (EFC) and ENTH/ANTH domains in the regulation of membrane-cytosol interfaces and membrane curvature. Biochim Biophys Acta *1761*, 897-912.

Itoh, T., Erdmann, K., Roux, A., Habermann, B., Werner, H., and De Camilli, P. (2005). Dynamin and the actin cytoskeleton cooperatively regulate plasma membrane invagination by BAR and F-BAR proteins. Dev Cell *9*, 791–804.

Ladokhin, A., Jayasinghe, S., and White, S. (2000). How to measure and analyze tryptophan fluorescence in membranes properly, and why bother. Anal Biochem *285*, 235-245.

Le Goff, L., Amblard, F., and Furst, E. M. (2002a). Motor-driven dynamics in actin-myosin networks. Phys Rev Lett *88*, 018101.

Le Goff, L., Hallatschek, O., Frey, E., and Amblard, F. (2002b). Tracer studies on f-actin fluctuations. Phys Rev Lett *89*, 258101.

Pettersen, E., Goddard, T., Huang, C., Couch, G., Greenblatt, D., Meng, E., and Ferrin, T. (2004). UCSF Chimera—A visualization system for exploratory research and analysis. Journal of Computational Chemistry *25*, 1605-1612.

Rodriguez, Y., Mezei, M., and Osman, R. (2007). Association free energy of dipalmitoylphosphatidylserines in a mixed dipalmitoylphosphatidylcholine membrane. Biophys J *92*, 3071-3080.

Schroeter, J. P., and Bretaudiere, J.-P. (1996). SUPRIM: Easily Modified Image Processing Software. Journal of Structural Biology *116*, 131-137.

Shimada, A., Niwa, H., Tsujita, K., Suetsugu, S., Nitta, K., Hanawa-Suetsugu, K., Akasaka, R., Nishino, Y., Toyama, M., Chen, L., *et al.* (2007). Curved EFC/F-BAR-Domain Dimers Are Joined End to End into a Filament for Membrane Invagination in Endocytosis. Cell *129*, 761-772.

Tsujita, K., Suetsugu, S., Sasaki, N., Furutani, M., Oikawa, T., and Takenawa, T. (2006). Coordination between the actin cytoskeleton and membrane deformation by a novel membrane tubulation domain of PCH proteins is involved in endocytosis

10.1083/jcb.200508091. J Cell Biol *172*, 269-279.

Valpuesta, J. M., Carrascosa, J. L., and Henderson, R. (1994). Analysis of electron microscope images and electron diffraction patterns of thin crystals of phi 29 connectors in ice. J Mol Biol *240*, 281-287.

Wang, L., Bose, P. S., and Sigworth, F. J. (2006). Using cryo-EM to measure the dipole potential of a lipid membrane. Proc Natl Acad Sci U S A *103*, 18528-18533.

Whittaker, M., Carragher, B. O., and Milligan, R. A. (1995). PHOELIX: a package for semi-automated helical reconstruction. Ultramicroscopy *58*, 245-259.

Wriggers, W., Milligan, R. A., and McCammon, J. A. (1999). Situs: A package for docking crystal structures into low-resolution maps from electron microscopy. J Struct Biol *125*, 185-195.

Zhang, P., and Hinshaw, J. E. (2001). Three-dimensional reconstruction of dynamin in the constricted state. Nat Cell Biol *3*, 922-926.

Chapter 3: DISCUSSION

Visualizing Membrane-Bound F-BARs: A Coat Composed of Shape-Based Scaffolds

Efforts to refine the mechanistic understanding of membrane remodeling by the BAR domain superfamily have been enhanced by the ability to visualize directly how select F-BARs interact with the bilayer, thus providing insight into the relative contributions of the scaffolding, amphipathic wedge, and oligomerization components of protein-induced membrane curvature. Cryo-electron microscopy techniques are uniquely suited for this area of research because they enable membranes to be observed under hydrated, near native conditions while fully preserving the structure and arrangement of membrane-associated and membrane-embedded proteins. When combined with digital image analysis for the alignment and averaging of different 2D projections, 3D reconstructions can be built to extract and interpret macromolecular information that is inaccessible to other structural methods. In addition, combining lower resolution reconstructions derived from cryo-electron microscopy with computationally-docked high-resolution crystal/NMR structures can lead to richly detailed views that span the spectrum from atoms to sub-cellular membranous organelles.

This work focused on the F-BAR modules found at the N-terminus of proteins from the Toca family (transducer of Cdc42-dependent actin assembly), namely Toca-3/CIP4 and Toca-2/FBP17 (Aspenstrom, 1997; Ho et al., 2004), whose structures have been solved (Shimada et al., 2007). By fitting the atomic models of these F-BARs into 3D reconstructions of membrane tubules generated *in vitro*, it was possible to observe directly how F-BARs employ a combination of scaffolding and collective coat formation to induce curvature. Specifically, the scaffolding hypothesis predicts that there should be resolvable points of contact between the phospholipid headgroups and clusters of cationic residues

found on the concave face of the F-BAR module, and that these contacts will constrain the membrane to match the curvature of the domain. Essentially proving this model, the reconstructions clearly resolved how four clusters of Lys and Arg residues on the surface of the F-BAR dimer mediate the attractive forces that enable these rigid dimers to impose their own shape on the underlying bilayer.

It was also observed that scaffolding by individual F-BARs was necessary but not sufficient, in that membrane tubule formation also required the collective assembly of F-BARs into a helical coat. This unique coat was held together by a tip-to-tip interaction—like the contact predicted by Shimada *et al.* based on crystal structures (Shimada et al., 2007)—as well as extensive lateral interactions. The broad, overlapping lateral interaction appeared to involve ~50% of the dimer's lateral surface, including the entire C-terminal extended peptide (Henne et al., 2007; Shimada et al., 2007). Fitting of the near-atomic models into the cryo-EM maps further suggested that specific contacts may have been important for the formation of the lateral interactions, including ionic and hydrophobic interactions between surface-exposed residues that have been conserved throughout the evolutionary history of the Toca proteins. A simple visual inspection of the twisted or "tilda" shape of the FCHo2 F-BAR module (Henne et al., 2007) suggests that these F-BARs may polymerize into a coat through similar lateral interactions. More generally, it is possible that every module of the BAR domain superfamily can oligomerize into a coat with specific architecture, whether through tip-to-tip or lateral interactions, and that oligomerization may enable different members of the BAR domain superfamily to distinguish self-similar domains during membrane remodeling. For example, it has been observed that F-BAR and N-BAR proteins will dynamically segregate from each other on membrane surfaces during membrane remodeling (Fig. 2-1 and (Itoh and De Camilli, 2006). Such segregation may be determined

in part by the affinity of a given BAR for a specific degree of curvature, but stereotyped protein-protein interactions may further endow different BARs with the ability to recruit self-similar modules to form discrete membrane microdomains.

Returning to the role of amphipathic "wedges", no such sequences have been identified within or flanking the F-BAR modules of Toca proteins, and there was no evidence at the resolution of the cryo-electron studies of amphipathic α-helices being intercalated into the outer leaflet of the bilayer. This is noteworthy, in that it has been largely assumed that the biological role of scaffolding domains, like BARs, is simply to stabilize an intrinsically-preferred degree of curvature that corresponds with the shape of module. In contrast, the intercalation of amphipathic α-helices has been considered as the primary driving force for inducing curvature *de novo* (Henne et al., 2007), as protein modules that do not appear to have a intrinsically-curved shape (e.g. Epsin and Sar1 proteins) can drive membrane curvature generation with amphipathic α-helices alone (Ford et al., 2002; Lee et al., 2005).

The cryo-electron studies did suggest that the membrane-bending energy and the energy liberated by membrane-binding of F-BAR scaffolds are of the same order of magnitude, in that simple manipulations of the temperature or varying the lipid composition could separate membrane-binding from membrane-bending. For example, lowering the temperature below the T_m of the principal lipid species (palmitoyl-oleyl phosphatidyl-serine, POPS)—a manipulation which presumably increased the rigidity of the membrane—inhibited tubule formation. Yet, F-BAR modules of the Toca family still avidly bound to these chilled membranes and formed oligomeric arrays in which laterally-adjacent dimers aligned in almost perfect register while forming the tip-to-tip contacts. In this state, the modules were lying on their sides via different cationic residues and thus could not directly

impose their concave faces on the membrane *or* form the lateral interactions required for helical coat assembly. Warming these membranes above their T_m to decrease the membrane-bending energy enabled the membrane to adopt the intrinsic curvature of the F-BAR's concave surface, and the flat membrane sheets were transformed into tubules. These observations further reinforced that F-BAR modules are more than simple curvature "sensors" or stabilizers; they readily bind to flat membranes and can generate curvature *de novo*. There is also no obvious justification for invoking membrane curvature-mediated attractive forces (Bruinsma and Pincus, 1996; Reynwar et al., 2007), since F-BAR dimers interact directly and extensively with each other on the surface of both flat and curved membranes. Perhaps F-BAR proteins have evolved to cluster together in limited oligomeric arrays on the surface of flat membranes, ready to induce membrane tubules in response to regulatory signals.

The Shape of Things to Come

As the control of membrane topology is fundamental to many essential cellular processes, there is a great need to study basic questions about the biology of the BAR domain superfamily and membrane remodeling in general. Remaining questions include the means by which cells regulate BAR domain function in time and space, targeting them to the appropriate membranes at the required times. For example, our current understanding of the mechanism of dimerization suggests that post-translational modifications or binding partners could inhibit the formation of the 6-helix bundle that defines the BAR fold. Similar mechanisms may be employed to regulate membrane-binding, as in the case of Arfaptin-2, where Rac or Arf binding to the concave surface likely blocks membrane binding. As noted earlier, BAR domains appear to non-specifically bind anionic lipid headgroups, and

synergistic partnerships with PH or PX domains are thought to provide specific targeting for some BAR proteins. However, *in vitro* analysis of lipid specificity may be inadequate evidence for this conclusion. Simple clusters of four or more K/R residues, like those found in BAR domains, have been shown *in vivo* to specifically interact with $PI(3,4,5)P_3$ and $PI(4,5)P_2$ (Heo et al., 2006). The non-specific interactions with anionic headgroups see *in vitro* with liposome preparations may not be comparable with *in vivo* conditions—especially given that electrostatics are sensitive to solution ionic strength and pH, equilibrium conditions *in vitro* which are unlikely to adequately mimic the cystol-membrane interface. Other means of regulation may come into play for each step of the higher-order oligomerization reactions, whether of helical coats or of discrete rings. Perhaps "capping" proteins will be discovered that prevent the formation of promiscuous coat interactions between BAR modules at inappropriate times. Finally, the developmental and physiological roles of most members of the BAR domain superfamily remain unknown.

Additional future goals should include an elucidation of the functional relationships between members of the BAR domain superfamily and other membrane-associated proteins. While the data presented here is focused on the membrane-molding properties of select F-BAR modules, like other branches of the BAR domain superfamily some F-BAR proteins have been shown to bind and modulate the function of the dynamin family of large GTPases (Itoh and De Camilli, 2006; Itoh et al., 2005). The first paper to describe the membrane-deforming properties of F-BAR domains also showed that their ability to induce tubule invaginations of the plasma membrane is antagonized by dynamins (Itoh et al., 2005), presumably though dynamin-mediated twisting and fission of the tubules (see Appendix I and (Roux et al., 2006). Moreover, F-BAR proteins that interact with dynamin have also been shown to regulate actin nucleation (Aspenstrom, 1997; Carnahan and Gould, 2003;

Coyle et al., 2004; Greer, 2002; Ho et al., 2004; Lippincott and Li, 1998; Lippincott and Li, 2000; Soderling et al., 2002), and there is strong evidence that the fissioning activity of dynamin requires an intact actin cytoskeleton (Itoh et al., 2005). Together, these observations hint at a fundamental but poorly understood regulatory network in the interplay between F-BAR protein-mediated 1) membrane invagination, 2) nucleation of actin fibers, and the fissioning of membrane tubules through 3) recruitment of dynamin-family GTPases (Itoh et al., 2005).

The evidence for such a regulatory system can be summarized as follows. Analysis of the domain organization and protein-protein interactions for many F-BAR proteins reveals that in addition to dimerizing to form F-BAR modules, these proteins often bind Rho-family GTPases or posses regulatory GAP modules for these enzymes. For the F-BAR proteins studied here, including Toca-1, Toca-2/FBP17 and Toca-3/CIP4, key links have been shown to exist with the GTPase Cdc42 and with N-WASP (Coyle et al., 2004; Ho et al., 2004; Kakimoto et al., 2006; Qualmann et al., 1999)—two critical and well-known players in Arp2/3-mediated actin nucleation at the membrane surface that also participate in endocytosis (Benesch et al., 2005; Garrett et al., 2000; Innocenti et al., 2005). Moreover, this subset of F-BAR proteins possess SH3 domains, which have been shown to bind to dynamins, synaptojanins, *and* members of the N-WASP/WAVE family (Itoh et al., 2005) as reviewed in (Itoh and De Camilli, 2006). These SH3-interacting proteins are known participants in either the remodeling of the actin-based cytoskeleton or the remodeling of the plasma membrane during endocytosis (Itoh and De Camilli, 2006); but whether each of these interactions is physiologically meaningful—and if they are meaningful whether there is a temporal sequence for these SH3 interactions that mirrors sequential endocytic stages—remains to be determined.

Insight into the mechanisms by which F-BAR proteins partner with other proteins in order to accomplish physiological processes like endocytosis may be found through further structural examinations of these proteins in their membrane-associated states. For example, do F-BAR proteins like FBP17 stably co-assemble with dynamin GTPases around membrane tubules? Or does FBP17 only transiently recruit dynamin to nascent tubules, and polymerization of the dynamin coat displaces the FBP17 coat? Considering the large difference in diameter between FBP17- and dynamin-coated tubules—as determined by the curvature and architecture of their respective coats—it seems unlikely that both proteins will be bound to adjacent membrane surfaces. However, there is some evidence that this may be possible and could be a mechanism by which FBP17 modulates the twistase activity of the dynamin coat (see Fig. 3-1 and (Itoh et al., 2005). If this is the case, there may be an analogy between F-BAR proteins and other members of the BAR domain superfamily, as there is considerable evidence that the "classical" BAR proteins endophilin (Farsad et al., 2001) and amphiphysin (Takei et al., 1999) can co-assemble with dynamin-1 on the surface of membrane tubules (see Fig. 3-2). As suggested by our analyses of these hybrid tubules and work done *in vitro* by other labs (Hill et al., 2001), co-polymerization of dynamin with endophilin may inhibit dynamin-mediated fission (see Fig. 3-2). The physiological significance of this finding is unclear, however, in that endophilin appears to be a required component of dynamin-dependent and clathrin-mediated endocytosis at synaptic terminals *in vivo* (Verstreken et al., 2002).

Fig. 3-1: Co-Assembly of FBP17 and Dynamin on Membrane Tubules

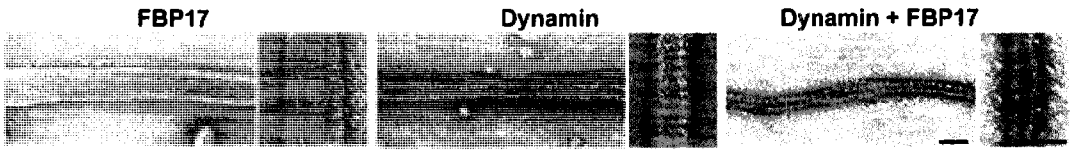

Liposomes incubated with full-length FBP17, with dynamin alone, or with both proteins. The presence of both was reported to induce the reorganization of the FBP17-only and dynamin-only coated tubules into narrower tubules decorated by a unique coat. Scale bar = 100 nm. Data generated by T. Itoh, figure adapted from (Itoh et al., 2005).

If full-length FBP17 is added to liposomes before dynamin-1, and the reaction is monitored by sequential negative staining after the addition of dynamin-1, distinct morphologies can be observed over the course of approximately one hour. The left and middle panels shown above were prepared 5 & 10 minutes, respectively, after the addition of dynamin-1 and 1mM GDP. The protein coat is disorganized and the underlying tubule shows regions of constriction versus relaxation, depending on the amount of bound protein. In the higher magnification middle panel there are no striations suggestive of a helical coat; but many large, globular protein particles can be seen decorating the outside edge of the tubule. After 1 hour, as shown in the right panel, the tubules look essentially like dynamin-only tubules with a high concentration of free protein in the surrounding solution. These observations are consistent with the hypothesis that dynamin-1 can displace FBP17 from the tubule surface.

Fig. 3-2: Co-Assembly of EndophilinA1 and Dynamin-1 on Membrane Tubules

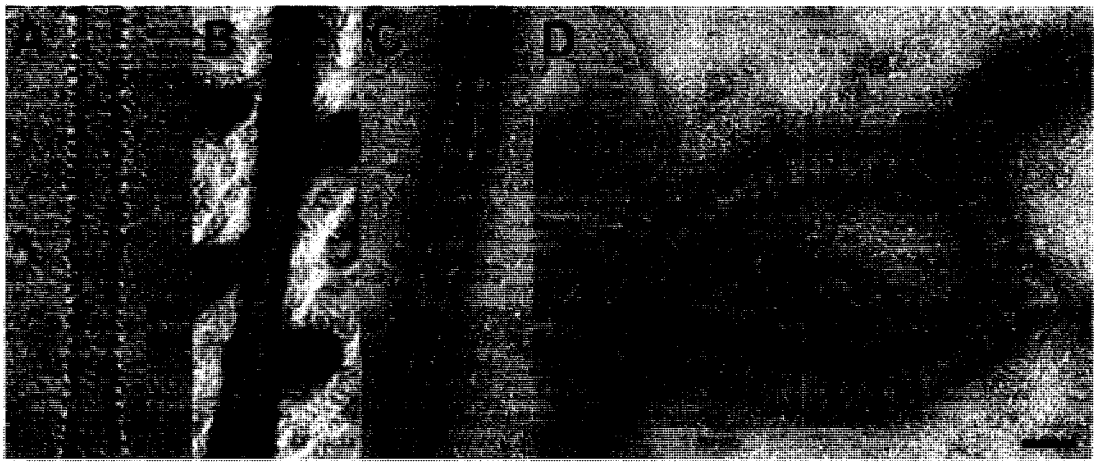

Some BAR superfamily proteins, like endophilin (Farsad et al., 2001) and amphiphysin (Takei et al., 1999), can stably co-assemble with dynamin-1 on membrane tubules. A) cryo-electron micrograph of an endophilinA1-only coated membrane tubule. B) electron micrograph of a negatively stained dynamin-1-only coated membrane tubule. C, D) electron micrographs of negatively stained endophilinA1+dynamin-1 coated tubules after 1 hour in the absence of nucleotides. Most notably, the longitudinal spacing between adjacent repeats of the helical coat expands in the hybrid coat. These observations are consistent with the hypothesis that the presence of the endophilin BAR domain prevents the mechano-chemical coupling required for the "twistase" activity of the dynamin-only protein coat. Bar = 50 nm.

As examination of Figs. 3-1 and 3-2 suggests, membrane-bound samples such as these must be improved before they will be amenable for 3D reconstruction. What is more, any structural investigations of the complexes formed between members of the BAR domain superfamily and either dynamins or actin nucleating factors will have to be complimented with dynamic assays of their function in real time *in vitro* and in living cells. Some structural features may simply be artifacts of reconstitution with model membranes in solution

conditions that do not adequately mirror the interface between the cytoplasm and the inner leaflet of the plasma membrane. A thermodynamic and kinetic assessment of the binding affinities for all of the putative SH3 domain interactions could be particularly useful to determine whether a protein like FBP17 can stably interact with a dynamin when confronted with alternative binding partners like N-WASP.

As suggested earlier, in addition to the implications for dynamin-dependent endocytosis, there is a great deal of interest and much to be learned about the interplay between the actin-based cytoskeleton and BAR-mediated membrane deformation. Factors that promote F-actin nucleation or stabilization appear to inhibit the accumulation of some BAR proteins on the membrane and tubulation in living cells, whereas pharmacological disruption of the actin-based cytoskeleton leads to dramatically enhanced tubulation by many members of the BAR domain superfamily (Itoh et al., 2005) & unpublished observations). In addition to being integral to dynamin-dependent and other modes of endocytosis, the link between BAR-domain driven membrane deformation and actin nucleation is fundamental to filopodia formation by I-BAR domain proteins and the structurally-distinct F-BAR domain of FNBP2 (unpublished observations). The link between membrane-deformation and actin nucleation is perhaps nowhere as dramatic as in the case of the formation of the cytokinetic actin ring and the invagination and ultimately fissioning of the plasma membrane during cell division. While there is not yet a clear example of a mammalian member of the BAR domain superfamily required for cytokinesis, in the model organism *S. pombe* two independent actin nucleation pathways, one dependent on the Arp2/3 complex and another involving the formin Cdc12p, both appear to be triggered by an F-BAR protein, Cdc15p, which directly links these actin-based structures to the cell membrane through its F-BAR domain (Carnahan and Gould, 2003).

Fig. 3-3: Cell Division in *S. pombe* Requires the F-BAR Protein Cdc15p

Image adapted from (Kanbe, 1989) of a thin section electron micrograph of a freeze-substituted *S. pombe* cell in the process of fissioning. Bar = 1 μm. The diameter of the membrane invaginations ranges from 50-80 nm (within the range of known BAR and F-BAR structures). Schematic representations of where the F-BAR domains of Cdc15p may localize have been overlaid in red. Small molecule inhibitors of the interaction between the F-BAR domain and the plasma membrane could be novel cell division inhibitors.

Are BAR Superfamily Domains "Druggable" Targets?

Seeking to understand how one protein, Cdc15p, simultaneously orchestrates the regulated assembly of a mechanically-intricate device like the cytokinetic actin ring *and* couples its constriction to the invagination and fissioning of the parent membrane is a fundamental pursuit of basic biology. What is more, if malignant cells utilize any members of the BAR domain superfamily during cell division, such investigations could lead to new therapeutic options in the fight against cancer. More broadly, pharmacological manipulation of members of the BAR domain superfamily represents new and completely uncharted terrain for cell biology and medicinal chemistry. The data presented in this thesis concerning the discrete and specific regions of electrostatic interaction between some F-BAR domains and their target membranes suggests that these contacts should be amenable to small-

molecule manipulation, and recent work in diverse fields suggests that this strategy has clinical merit. Beyond cell division, some malignancies form cellular extensions that enable metastatic migration and invasion—podosomes or so-called "invadopodia" (Linder, 2007)—and at least one BAR protein, ASAP1, is required for invadopodia formation (Bharti et al., 2007). Metabolically, new work has shown that a complex formed between the VPS9 domain-containing protein Gapex-5 and the F-BAR protein CIP4 is essential for insulin-stimulated GLUT4 translocation (Hou and Pessin, 2007; Lodhi et al., 2007), and that CIP4 KO animals are unable to internalize GLUT4 from the plasma membrane (unpublished observations of S. Corey, personal communication). Small molecule inhibition of CIP4-mediated internalization of GLUT4 is therefore a novel strategy for treating insulin resistance and diabetes mellitus. Finally, testicular Sertoli cells contain tubular invaginations of the plasma membrane that transiently form at points of contact with maturing spermatids. Recent work has shown that both amphiphysin-1 and dynamin-2 mediate formation of these tubules and are required for spermatid maturation and release, hinting that long-sought-after male contraceptives could be found in the search for specific BAR domain inhibitors (Kusumi et al., 2007).

Concluding Remarks

In conclusion, the experiments presented here are important first steps toward the structural exploration of membrane remodeling. Future efforts to elucidate the biology of the BAR domain superfamily and to develop pharmacological probes that modulate their function for research and therapy will benefit from the advancements reported here.

References

Aspenstrom, P. (1997). A Cdc42 target protein with homology to the non-kinase domain of FER has a potential role in regulating the actin cytoskeleton. Current Biology *7*, 479-487.

Benesch, S., Polo, S., Lai, F. P., Anderson, K. I., Stradal, T. E., Wehland, J., and Rottner, K. (2005). N-WASP deficiency impairs EGF internalization and actin assembly at clathrin-coated pits. J Cell Sci *118*, 3103-3115.

Bharti, S., Inoue, H., Bharti, K., Hirsch, D. S., Nie, Z., Yoon, H. Y., Artym, V., Yamada, K. M., Mueller, S. C., Barr, V. A., and Randazzo, P. A. (2007). Src-dependent phosphorylation of ASAP1 regulates podosomes. Mol Cell Biol *27*, 8271-8283.

Bruinsma, R., and Pincus, P. (1996). Protein aggregation in membranes. Current Opinion in Solid State & Materials Science *1*, 401-406.

Carnahan, R. H., and Gould, K. L. (2003). The PCH family protein, Cdc15p, recruits two F-actin nucleation pathways to coordinate cytokinetic actin ring formation in Schizosaccharomyces pombe. J Cell Biol *162*, 851-862.

Coyle, I. P., Koh, Y. H., Lee, W. C., Slind, J., Fergestad, T., Littleton, J. T., and Ganetzky, B. (2004). Nervous wreck, an SH3 adaptor protein that interacts with Wsp, regulates synaptic growth in Drosophila. Neuron *41*, 521-534.

Farsad, K., Ringstad, N., Takei, K., Floyd, S. R., Rose, K., and De Camilli, P. (2001). Generation of high curvature membranes mediated by direct endophilin bilayer interactions. J Cell Biol *155*, 193-200.

Ford, M. G., Mills, I. G., Peter, B. J., Vallis, Y., Praefcke, G. J., Evans, P. R., and McMahon, H. T. (2002). Curvature of clathrin-coated pits driven by epsin. Nature *419*, 361-366.

Garrett, W. S., Chen, L. M., Kroschewski, R., Ebersold, M., Turley, S., Trombetta, S., Galan, J. E., and Mellman, I. (2000). Developmental control of endocytosis in dendritic cells by Cdc42. Cell *102*, 325-334.

Greer, P. (2002). Closing in on the biological functions of Fps/Fes and Fer. Nat Rev Mol Cell Biol *3*, 278-289.

Henne, W. M., Kent, H. M., Ford, M. G. J., Hegde, B. G., Daumke, O., Butler, P. J. G., Mittal, R., Langen, R., Evans, P. R., and McMahon, H. T. (2007). Structure and Analysis of FCHo2 F-BAR Domain: A Dimerizing and Membrane Recruitment Module that Effects Membrane Curvature. Structure *15*, 1-14.

Heo, W. D., Inoue, T., Park, W. S., Kim, M. L., Park, B. O., Wandless, T. J., and Meyer, T. (2006). PI(3,4,5)P3 and PI(4,5)P2 Lipids Target Proteins with Polybasic Clusters to the Plasma Membrane

10.1126/science.1134389. Science *314*, 1458-1461.

Hill, E., van der Kaay, J., Downes, C. P., and Smythe, E. (2001). The Role of Dynamin and Its Binding Partners in Coated Pit Invagination and Scission

10.1083/jcb.152.2.309. J Cell Biol *152*, 309-324.

Ho, H. Y., Rohatgi, R., Lebensohn, A. M., Le, M., Li, J., Gygi, S. P., and Kirschner, M. W. (2004). Toca-1 mediates Cdc42-dependent actin nucleation by activating the N-WASP-WIP complex. Cell *118*, 203-216.

Hou, J. C., and Pessin, J. E. (2007). Ins (endocytosis) and outs (exocytosis) of GLUT4 trafficking. Curr Opin Cell Biol *19*, 466-473.

Innocenti, M., Gerboth, S., Rottner, K., Lai, F. P., Hertzog, M., Stradal, T. E., Frittoli, E., Didry, D., Polo, S., Disanza, A., *et al.* (2005). Abi1 regulates the activity of N-WASP and WAVE in distinct actin-based processes. Nat Cell Biol *7*, 969-976.

Itoh, T., and De Camilli, P. (2006). BAR, F-BAR (EFC) and ENTH/ANTH domains in the regulation of membrane-cytosol interfaces and membrane curvature. Biochim Biophys Acta *1761*, 897-912.

Itoh, T., Erdmann, K., Roux, A., Habermann, B., Werner, H., and De Camilli, P. (2005). Dynamin and the actin cytoskeleton cooperatively regulate plasma membrane invagination by BAR and F-BAR proteins. Dev Cell *9*, 791–804.

Kakimoto, T., Katoh, H., and Negishi, M. (2006). Regulation of neuronal morphology by Toca-1, an F-BAR/EFC protein that induces plasma membrane invagination. J Biol Chem *281*, 29042-29053.

Kanbe, T. (1989). Dynamics of cytoplasmic organelles in the cell cycle of the fission yeast Schizosaccharomyces pombe: three-dimensional reconstruction from serial sections. In Journal of Cell Science, pp. 647-656.

Kusumi, N., Watanabe, M., Yamada, H., Li, S.-A., Kashiwakura, Y., Matsukawa, T., Nagai, A., Nasu, Y., Kumon, H., and Takei, K. (2007). Implication of Amphiphysin 1 and Dynamin 2 in Tubulobulbar Complex Formation and Spermatid Release. Cell Structure and Function *32*, 101-113.

Lee, M. C. S., Orci, L., Hamamoto, S., Futai, E., Ravazzola, M., and Schekman, R. (2005). Sar1p N-Terminal Helix Initiates Membrane Curvature and Completes the Fission of a COPII Vesicle. Cell *122*, 605-617.

Linder, S. (2007). The matrix corroded: podosomes and invadopodia in extracellular matrix degradation. Trends Cell Biol *17*, 107-117.

Lippincott, J., and Li, R. (1998). Dual function of Cyk2, a cdc15/PSTPIP family protein, in regulating actomyosin ring dynamics and septin distribution. J Cell Biol *143*, 1947-1960.

Lippincott, J., and Li, R. (2000). Involvement of PCH family proteins in cytokinesis and actin distribution. Microscopy Research and Technique *49*, 168-172.

Lodhi, I. J., Chiang, S. H., Chang, L., Vollenweider, D., Watson, R. T., Inoue, M., Pessin, J. E., and Saltiel, A. R. (2007). Gapex-5, a Rab31 guanine nucleotide exchange factor that regulates Glut4 trafficking in adipocytes. Cell Metab *5*, 59-72.

Qualmann, B., Roos, J., DiGregorio, P. J., and Kelly, R. B. (1999). Syndapin I, a synaptic dynamin-binding protein that associates with the neural Wiskott-Aldrich syndrome protein. Mol Biol Cell *10*, 501-513.

Reynwar, B. J., Illya, G., Harmandaris, V. A., Muller, M. M., Kremer, K., and Deserno, M. (2007). Aggregation and vesiculation of membrane proteins by curvature-mediated interactions. Nature *447*, 461-464.

Roux, A., Uyhazi, K., Frost, A., and De Camilli, P. (2006). GTP-dependent twisting of dynamin implicates constriction and tension in membrane fission. Nature *441*, 528-531.

Shimada, A., Niwa, H., Tsujita, K., Suetsugu, S., Nitta, K., Hanawa-Suetsugu, K., Akasaka, R., Nishino, Y., Toyama, M., Chen, L., *et al.* (2007). Curved EFC/F-BAR-Domain Dimers Are Joined End to End into a Filament for Membrane Invagination in Endocytosis. Cell *129*, 761-772.

Soderling, S. H., Binns, K. L., Wayman, G. A., Davee, S. M., Ong, S. H., Pawson, T., and Scott, J. D. (2002). The WRP component of the WAVE-1 complex attenuates Rac-mediated signalling. Nat Cell Biol *4*, 970-975.

Takei, K., Slepnev, V. I., Haucke, V., and De Camilli, P. (1999). Functional partnership between amphiphysin and dynamin in clathrin-mediated endocytosis. Nat Cell Biol *1*, 33-39.

Verstreken, P., Kjaerulff, O., Lloyd, T. E., Atkinson, R., Zhou, Y., Meinertzhagen, I. A., and Bellen, H. J. (2002). Endophilin Mutations Block Clathrin-Mediated Endocytosis but Not Neurotransmitter Release. Cell *109*, 101-112.

Appendix I: GTP-Dependent Twisting of Dynamin

Implicates Constriction and Tension in Membrane Fission

This appendix is adapted from Roux, A., Uyhazi, K., Frost, A., and De Camilli, P. (2006). **Nature** *441*, 528-531. A.R. and P.D.C. conceived the project, designed the experiments and evaluated the results. A.R. performed the experiments alone, with the exception of the giant-liposome assay (K.U. and A.R.), and electron microscopy (A.F. and A.R.). A.R. and P.D.C. wrote the original paper.

Dynamin is a GTPase which genetic studies have strongly implicated in the fission reaction of endocytosis (De Camilli et al., 1995; Hinshaw, 2000; Sever et al., 2000). It is a member of a family of GTPases that participate in membrane fission by oligomerizing into spirals (Hinshaw and Schmid, 1995; Ingerman et al., 2005; Takei et al., 1995) around sites of membrane constriction (Takei et al., 1995). Dynamin was initially proposed to act as a mechanoenzyme that constricts and cuts the neck of nascent vesicles in a GTP-hydrolysis-dependent reaction (Hinshaw and Schmid, 1995; Takei et al., 1995), but subsequent studies have suggested alternative models (Sever et al., 1999; Stowell et al., 1999). To directly test these models of dynamin function, Aurélien Roux developed microscopy assays to monitor the real-time effect of nucleotides on dynamin coated lipid tubules. Addition of GTP, but not of GDP or GTPγS, to the tubules resulted in their twisting, as visualized by light and electron microscopy, suggesting that the turns of the dynamin helix undergo a rotary movement relative to each other during GTP hydrolysis. Rotation of dynamin around the longitudinal axis of the tubules was confirmed by the movement of streptavidin beads attached to biotin-dynamin coated tubules. Twisting activity produced a longitudinal contraction of the tubules that was released by tubule break and resulted in supercoiling. These findings strongly support a mechanoenzyme activity of dynamin in membrane fission, although they demonstrate that ring constriction triggered by GTP is not sufficient for fission. We suggest that the numerous interactors of dynamin (Praefcke and McMahon, 2004; Slepnev and De Camilli, 2000; Soulet et al., 2005), including components of the actin cytoskeleton (Cao et al., 2003; Itoh et al., 2005; Qualmann et al., 2000), may cooperate with the constricting and twisting activity of dynamin to produce a force leading to fission.

Purified dynamin was shown by negative staining electron microscopy to tubulate lipid membranes and to constrict and fragment them into small vesicles upon GTP hydrolysis (Sweitzer and Hinshaw, 1998; Takei et al., 1999). Subsequently, however, when the products of these incubations were analyzed by cryo-EM, GTP-dependent constriction, but not fission, was observed (Danino et al., 2004). It was proposed that the fragmentation observed in some studies resulted from mechanical stress of the constricted tubules during the manipulations involved in sample preparation. A major limitation of EM methods for the analysis of dynamin action in cell-free systems is that they rely on static observations. To overcome this limitation, we developed a light microscopy-based *in vitro* system that allows dynamic monitoring of dynamin dependent tubulation and fission of lipid membranes.

We adapted a previously described method for the analysis of polymer-dependent membrane deformation (Tsafrir et al., 2003). A drop of lipids is first deposited and dried on a coverslip, which is then mounted with thin spacers on a glass slide to create a microchamber. Addition of buffers produces a reorganization of the lipids into stacks of flat membrane bilayers (see Appendix II) that we used as templates for membrane tubulation by purified dynamin. As lipids, either a Brain Polar Lipids (BPL) fraction or a Synthetic Lipids Mixture (SLM) mimicking BPL (see see Appendix II), both supplemented with 5% m/m PtdIns(4,5)P_2, were used. Injection of purified brain dynamin (0.4-1 mg/ml in the absence of nucleotides) into the chamber induced the growth of narrow tubules which could be observed by Differential Interference Contrast (DIC) microscopy. Many of the tubules started to grow perpendicularly to the membrane plane, then collapsed on it, thus forming a two-dimensional network on the most superficial membrane sheet (Fig.1A, arrowheads). Other tubules grew at the very edge, and away from the sheets (Fig, 1A and 1C). Tubulation was less efficient with a decrease in the PS/PC ratio in the lipid mixture (not shown) and

Fig. AI-1: Generation and growth of dynamin-coated membrane tubules.

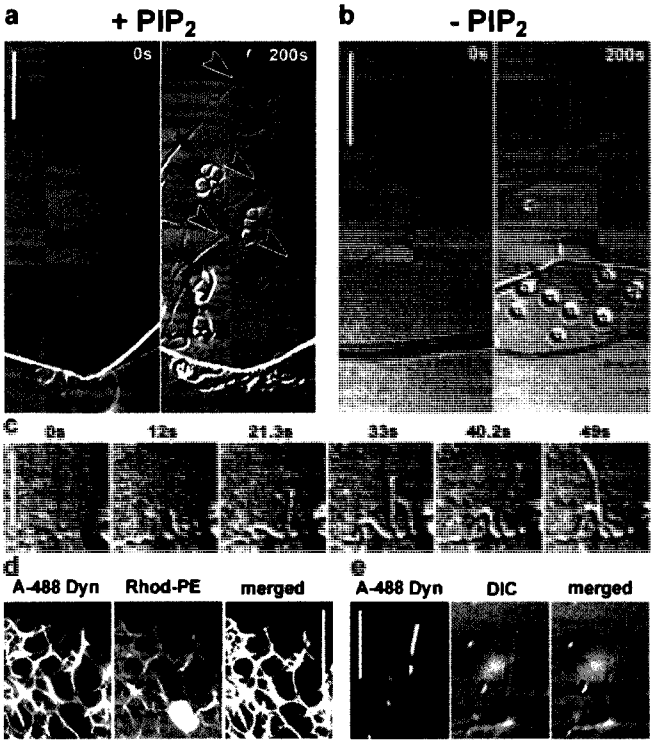

A) DIC microscopy images showing the effect of dynamin (1mg/ml) on membrane sheets composed of SLM (see Materials and Methods). 200 secs after dynamin addition, a two-dimensional network of tubules is visible (red arrowheads). B) Same as in A but without PtdIns(4,5)P_2. Blue arrows present in both A and B point to lipid sheet deformations produced by the glycerol present in the dynamin solution. C) Time lapse sequence showing growth of a single dynamin-coated tubule. D) Double fluorescence of a tubule network generated by Alexa 488 dynamin (A-488 Dyn) on membrane sheets (SLM) doped with a fluorescent phospholipid (Rhod-PE). E) Fluorescence and DIC microscopy images of a tubule generated by the sequential addition (approximately 15 sec interval) of Alexa 488 dynamin and unlabeled dynamin. Fluorescence marks the older portions of the coat. s, seconds. Scale bars, 10 μm in A, B and D; 2 μm in C; 5 μm in E.

required presence of PtdIns(4,5)P_2 (compare Fig. 1A with Fig. 1B). Tubules grew at the rate of approx 5-7 μm/min (Fig. 1C) and up to tens of micrometers (Fig. 1A), eventually forming an apparent network (Fig. 1D). Fluorescence experiments involving lipids doped with Rhodamine-dioleylPhosphatidylEthanolamine (Rhod-PE) and Alexa 488-conjugated dynamin confirmed that the linear structures visible by DIC microscopy were indeed dynamin coated membrane tubules (Fig 1D).

Sequential injection of Alexa 488-dynamin and unlabeled dynamin revealed lack of random molecular intermixing within the coat. When fluorescent dynamin was injected first, most fluorescent lipid segments were found at the tubule tips, suggesting that tubules grew from their base (Fig. 1E). However, several fluorescent segments bracketed by unlabeled segments were also seen (Fig. 1E), possibly reflecting polymerization of unlabeled dynamin from points of discontinuity within the dynamin coat.

We next investigated the effect of nucleotide on the tubules. 1 mM GTP led to a rapid reorganization of the tubule network. Most tubules first became straight (within seconds), suggesting contraction and longitudinal stretching between nodes of the network. Then, they broke and collapsed, leading to complete disruption (within 10-20 secs) of the network and to isolated clusters of membranes (Fig. 2A). GDP injection caused only a light contraction of the network, but no fission (Fig 2B). GTPγS, a non-hydrolysable analog of GTP, did not produce either contraction or fission, and stimulated the growth of new tubes (Fig. 2B). Similar results were obtained using Alexa 488-dynamin and Rhod-PE labeled lipids. Both fluorescent dyes underwent the same changes detected by DIC (Fig. 2C), thus confirming that lipid tubule disruption by GTP is not the result of dynamin dissociation from the lipids in the presence of this nucleotide.

Fig. AI-2: Effect of guanylnucleotides on the dynamin coated lipid tubules.

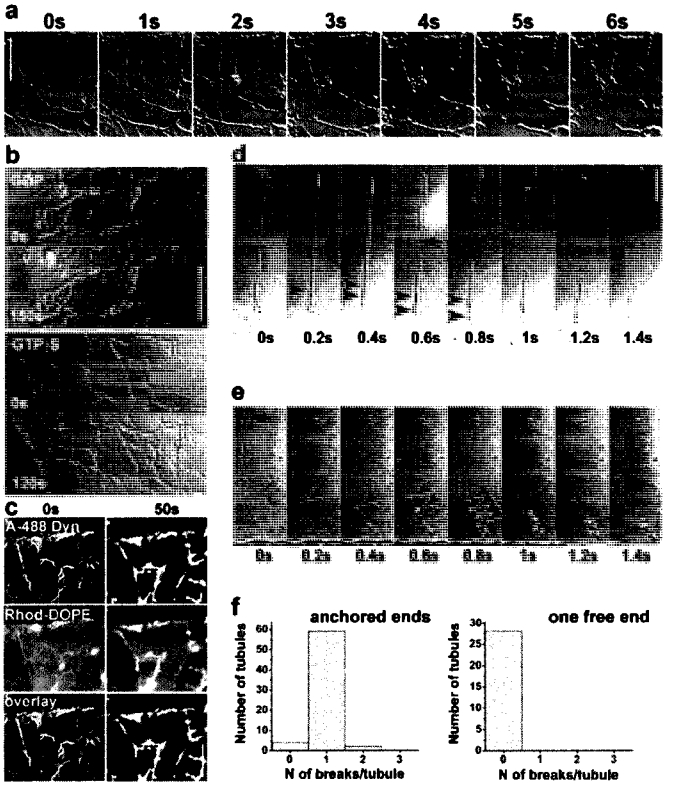

A) Time lapse series (DIC microscopy) showing that 1 mM GTP induces rapid (within secs) fragmentation of the tubule network. B), No fragmentation is observed 150 secs after the addition of 1 mM GTPγS and 1 mM GDP, respectively. C) Double fluorescence of dynamin (A-488 Dyn) coated tubules on Rhod-PE labeled membrane sheets at 0 and 50 secs after 1mM GTP injection, showing that dynamin does not dissociate from the lipid fragments. D, E) DIC microscopy time-lapse sequences of two dynamin-coated membrane tubule upon exposure to 1mM GTP. In D, the tubule became straight before a single break (blue arrow), suggesting the onset of tension between anchoring points at both ends of the tubule. In E, the tubule retracted. Observation of this tubule before GTP addition revealed motion of one of its two ends (blue arrow), indicating no anchorage at this end. Red arrows in D and E point to focal densities which appear along the tubules as they contract (D) or retract (E). F) Statistics of breaks for tubules whose contraction was constrained or non constrained by the apparent presence of anchorage points at both ends. For A and B, a SLM containing 50% POPS and 15 % POPC was used. In all other cases, the standard SLM was used. s, seconds. Scale bars, 10 μm in a-c; 5 μm in D and E.

To gain a better insight into the sequence of events leading to tubule contraction and break, the behavior of many individual tubules following GTP addition was examined. Increase in longitudinal tension, as indicated by the acquisition of a tight rectilinear course (Fig. 2A and 2D), often correlated with the appearance of densities along the tubule (arrowheads in Fig. 2D, see discussion below) and ended with a single break that released tension and was followed by the retraction of the two stumps (Fig. 2D). In contrast, when tubules seemed to be free from anchorage points other than their origin, they retracted without any break (Fig. 2E). As revealed by a morphometric analysis, almost no exception to this rule was observed (Fig. 2F). Similar results were observed by fluorescence microscopy of Rhod-PE and Alexa 488-dynamin labeled tubules (not shown), thus proving that breaks involve both the lipid tubules and their dynamin coat. These findings indicate that the constricting activity of dynamin is insufficient to achieve fission and that, at least under these *in vitro* conditions, longitudinal tension must come into play. They also demonstrate that dynamin can generate such tension, possibly by a contracting activity of the coat, which is antagonized by anchorage points at the two ends of the tubule. In fact, cryo-EM analysis (Chen et al., 2004; Danino et al., 2004; Zhang and Hinshaw, 2001) of lipid tubules coated by dynamin in the dilated state and in the constricted state revealed that constriction also results in a reduction of the helical pitch (from 13 nm to 9 nm (Danino et al., 2004)), thus producing an approximately 30% shortening of the dynamin helix. One could expect that, if tubules were anchored at multiple sites along their length, multiple fission events would occur.

To address this question, we investigated the effect of dynamin on preformed tubules with multiple anchorage points to a substrate, using a different *in vitro* assay. Lipid tubules were generated by depositing giant liposomes doped with Rhod-PE onto a network

of microtubules in the presence of kinesin and ATP (Fig. 3A, left panel), as previously described (Roux et al., 2002). The medium was then replaced by an ATP-free buffer to lock kinesin in the microtubule-bound state, thus leading to many attachment sites of the lipid tubules onto microtubules. Dynamin, or Alexa 488 dynamin, was then added. As seen by fluorescence, dynamin did associate with the lipid tubules, and, consistent with its microtubule binding properties (Shpetner and Vallee, 1989), also with microtubules (Fig. 3A, middle panels). Under these conditions, dynamin did not produce fission events, although it appeared to produce tubule constriction with focal swelling (data not shown and Fig. 3A, middle panels). This constriction is in agreement with the smaller diameters of dynamin coated tubules (about 20 nm (Chen et al., 2004)) relative to kinesin-pulled tubules (in the range of 40 nm or more) (Roux et al., 2002). Upon GTP addition, however, lipid tubules were rapidly cut into small fragments (Fig. 3A, right panels, Fig. 3B), some of which floated away into the medium, possibly reflecting the slow reversibility of kinesin-microtubule attachment sites (Fig. 3B, arrowheads). Dynamin, as expected (Maeda et al., 1992), dissociated from microtubules although it remained associated with the lipid fragments (Fig. 3A, center and right panel). Hence, when tubules have multiple attachment sites to a substrate (microtubules in this case), the activity of dynamin produce multiple fission events.

While longitudinal contraction may explain fragmentation of anchored lipid tubules, it is not sufficient to account for the significant contraction/retraction observed for free tubules in the membrane sheet assay (see for example Fig. 2E). A potential mechanism for such a dramatic contraction came from further observation of tubule dynamics upon GTP addition. In several cases, dynamin coated tubules formed loops (Fig. 4A). Upon GTP addition, these loops underwent twisting to form supercoiled structures (plectonemes, red arrows, Fig 4A and Fig. 5 electron micrographs), suggesting an underlying twisting of the

Fig. AI-3: Dynamin dependent fission of membrane tubules generated by kinesin on a microtubule network.

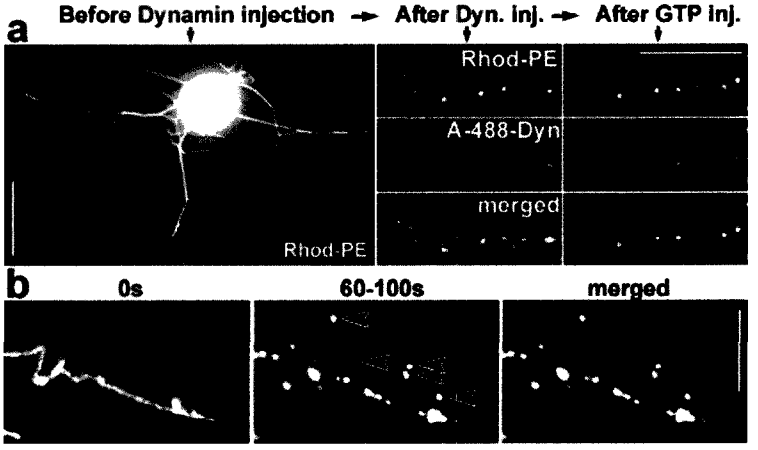

A, Fluorescence images of membrane tubules which were generated from giant liposomes [brain polar lipids doped with Rhod-PE plus 5% PtdIns(4,5)P_2] on a network of microtubules in the presence of kinesin. The area indicated by a red box is shown at higher magnification in the middle panels after the wash-out of ATP and addition of Alexa 488-dynamin (1 mg/ml). Tubule constriction with focal swelling, but no fission, can be observed. Note that fluorescent dynamin (A-488 Dyn) is associated both with membrane tubules and with microtubules (red arrows), consistent with its microtubule binding properties. Upon addition of 1mM GTP (right panels), tubules, which were anchored at multiple points on the microtubules by kinesin, underwent fragmentation into small vesicles. B) Fluorescent images showing a lipid tubule before (left panel) and after (center panel) the addition of GTP. The right panel show a merge of the two fields in pseudocolors. In the middle panel, 20 frames from 60 to 100 secs were superimposed to show diffusion of some lipid fragments (red arrowheads) away from the microtubules and thus proving the occurrence of fission. In this superimposition of many images (50 msec exposure, 2 sec time lapse), only some lipid fragments were visualized because, due to their rapid motility, only some of them could be captured by the time lapse. The diffusion of some of the lipid particles away from microtubules most likely reflects a slow dissociation of kinesin from microtubules. Bars = 5 μm.

dynamin coat itself. Supercoiling would explain retraction of free tubules and dense spots appearing on tubules during their contraction and/or retraction (red arrowheads in Fig. 2D and E) may represent supercoils. We explored the possibility of monitoring directly the twisting activity of the tubules by appending to them a reference point detectable by video-microscopy. Partial rotations of each turn of the helix over the adjacent one will result in complete rotations when compounded over many turns along the tubule. Tubules were generated with biotinylated dynamin (see Appendix II) in the presence of streptavidin-coated latex beads (260 nm in diameter). DIC microscopy, followed by computational analysis, was then used to track the motility of beads on tubules that connected the lipid sheets to an anchoring point on the glass slide. No motility was observed before GTP addition. GTP, after a lag phase explained at least in part by its diffusion into the microchamber, triggered both tubule tension and a striking oscillatory movement of the beads, strongly suggestive of rotations around the longitudinal axis of the tubule (Fig. 4B,C). As many as 30 rotations were observed for an individual bead, with the speed of rotation decreasing with the number of rotations until the break occurred (Fig 4C,D). Furthermore, the average maximal speed of bead rotation increased with the GTP concentration (Fig. 4C,E).

These results show that dynamin, during GTP hydrolysis, generates a rotational force on lipid tubules, which in turn leads to tubules contraction (and supercoiling), and thus to fission if contraction is antagonized by opposing forces. They suggest that the dynamin helix acts as a spiral undergoing further torsion upon GTP hydrolysis. In support of this possibility, electron microscopy of dynamin coated tubules that had been reacted with GTP in suspension and subsequently applied to EM grids, revealed supercoils (Fig. 4F and Fig. 5). This result is consistent the "convoluted" appearance previously noted for tubules prepared in similar conditions in another study (Danino et al., 2004). All these supercoils had "plus"

configuration (Fig. 4F), as expected from a right-handed twist (Charvin et al., 2003). Since dynamin is a right-handed helix (Zhang and Hinshaw, 2001), a right-handed twist will further coil the helix (see Fig. 4G). Increased coiling is consistent with previous observations made by cryo-electron microscopy: i) snapshots of dynamin 1 in the constricted state reveals fewer repeating units per turn than dynamin in the dilated state (Chen et al., 2004) and ii) both the inner diameter and the pitch of the helix decrease with GTP hydrolysis (Danino et al., 2004). The increase in the pitch of the dynamin helix observed upon GTP hydrolysis in one study (Stowell et al., 1999), may reflect the rigidity of the lipid nanotubes used as the lipid templates in that study. Under these conditions, the resistance to twisting opposed by the template may induce a distortion of the dynamin helix.

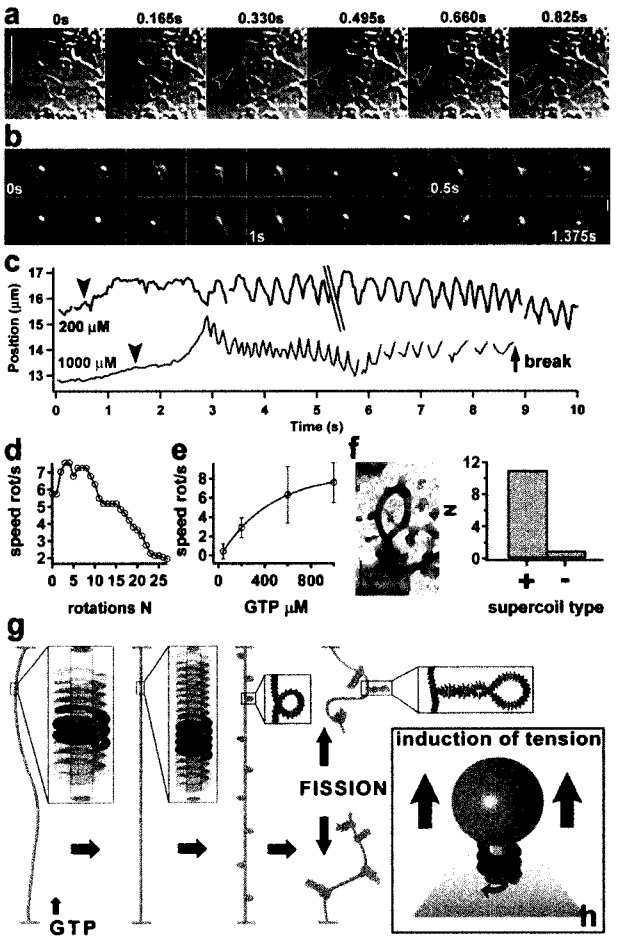

Fig. AI-4: Twisting activity of the dynamin coat.

A, Time-lapse images (DIC microscopy) showing that loops of dynamin coated tubules undergo supercoiling (red arrowheads) upon the addition of GTP (1 mM). B) Effect of GTP (200 µM) on tubules generated by biotinylated dynamin in the presence of streptavidin-coated latex beads. The time-lapse shows that the addition of the nucleotide triggers rotation of a

bead around the tubule. C) Tracking of the movement of single beads in experiments carried out with two different GTP concentrations. The displacement shown represents movements perpendicular to the main axis of the tubules. Green arrowheads show GTP addition. D) Instantaneous angular speed (rotations/second) of one of the two beads tracked in C' (1 mM experiment) versus the number (N) of rotations. E) Average maximal angular speed of the beads as a function of the GTP concentration. F) Electron microscopy image of a dynamin-coated tubule incubated with GTP (200 μM) prior to absorption onto an EM grid. Note its "plus" supercoiled structure (plectoneme), consistent with the right-handed coil of a right handed helix. Morphometric analysis demonstrated that the majority of plectonemes have a plus configuration. G) Schematic diagram of the effect of GTP on dynamin coated tubules. After GTP addition, the dynamin helix undergoes an increase in torsion leading to straighteneing of the tubule and supercoiling until a break occurs allowing more supercoiling. H) Proposed synergy between the twisting action of dynamin, which participates in constriction, and factors that promote the movement of the nascent vesicle away from the plasma membrane, which produce tension, in the fission of an endocytic vesicle. Scale bars, 10 μm in A; 1 μm in B; 200 nm in F.

Fig. AI-5: EM Evidence of the Twisting Activity of the Dynamin Coat

Electron micrographs of dynamin-coated tubules incubated with GTP (200 μM) for 2 minutes prior to absorption onto EM grids and staining with uranyl formate. These images are direct visualizations of the schematic diagrams shown in Fig 4G of the effect of GTP on dynamin coated tubules. After GTP addition, the dynamin helix undergoes an increase in torsion leading to supercoiling.

Collectively, the findings reported here provide strong support to the hypothesis that dynamin, and most likely other dynamin-like proteins implicated in membrane fission, function as mechanoenzymes. They demonstrate that the GTPase activity of polymerized dynamin spirals produce a twisting activity that cooperates with conformational changes in dynamin to constrict the underlying membrane tubule. In the case of the lipid tubules used here as a model system, this twisting activity also contributes to a longitudinal contraction that has been helpful to establish the requirement of membrane tension in dynamin-mediated fission. In the case of a nascent endocytic vesicle, where dynamin may form only a very short spiral, other factors may participate in the induction of tension along the axis of the tubular neck of the vesicle (Fig. 4H). Strong biochemical (Cao et al., 2003; Itoh et al.,

2005; Qualmann et al., 2000) and functional (Itoh et al., 2005; Lee and De Camilli, 2002; Merrifield et al., 2005) evidence has shown that the actin cytoskeleton acts together with dynamin in endocytic fission. Actin-based mechanisms, which were proposed to propel nascent endocytic vesicles away from the plasma membrane, may provide such tension (Kaksonen et al., 2005; Merrifield et al., 2005). We suggest that a cooperation of mechanisms which mediate constriction with mechanisms that create membrane tension may represent a general phenomenon in membrane fission (Roux et al., 2005), even though the players implicated in the generation of constriction and tension may differ in different contexts.

References

Cao, H., Orth, J. D., Chen, J., Weller, S. G., Heuser, J. E., and McNiven, M. A. (2003). Cortactin is a component of clathrin-coated pits and participates in receptor-mediated endocytosis. Mol Cell Biol *23*, 2162-2170.

Charvin, G., Bensimon, D., and Croquette, V. (2003). Single-molecule study of DNA unlinking by eukaryotic and prokaryotic type-II topoisomerases. Proc Natl Acad Sci U S A *100*, 9820-9825.

Chen, Y. J., Zhang, P., Egelman, E. H., and Hinshaw, J. E. (2004). The stalk region of dynamin drives the constriction of dynamin tubes. Nat Struct Mol Biol *11*, 574-575.

Danino, D., Moon, K. H., and Hinshaw, J. E. (2004). Rapid constriction of lipid bilayers by the mechanochemical enzyme dynamin. J Struct Biol *147*, 259-267.

De Camilli, P., Takei, K., and McPherson, P. S. (1995). The function of dynamin in endocytosis. Curr Opin Neurobiol *5*, 559-565.

Hinshaw, J. E. (2000). Dynamin and its role in membrane fission. Annu Rev Cell Dev Biol *16*, 483-519.

Hinshaw, J. E., and Schmid, S. L. (1995). Dynamin self-assembles into rings suggesting a mechanism for coated vesicle budding. Nature *374*, 190-192.

Ingerman, E., Perkins, E. M., Marino, M., Mears, J. A., McCaffery, J. M., Hinshaw, J. E., and Nunnari, J. (2005). Dnm1 forms spirals that are structurally tailored to fit mitochondria. J Cell Biol *170*, 1021-1027.

Itoh, T., Erdmann, K., Roux, A., Habermann, B., Werner, H., and De Camilli, P. (2005). Dynamin and the actin cytoskeleton cooperatively regulate plasma membrane invagination by BAR and F-BAR proteins. Dev Cell, in press.

Kaksonen, M., Toret, C. P., and Drubin, D. G. (2005). A modular design for the clathrin- and actin-mediated endocytosis machinery. Cell *123*, 305-320.

Lee, E., and De Camilli, P. (2002). Dynamin at actin tails. Proc Natl Acad Sci U S A *99*, 161-166.

Maeda, K., Nakata, T., Noda, Y., Sato-Yoshitake, R., and Hirokawa, N. (1992). Interaction of dynamin with microtubules: its structure and GTPase activity investigated by using highly purified dynamin. Mol Biol Cell *3*, 1181-1194.

Merrifield, C. J., Perrais, D., and Zenisek, D. (2005). Coupling between clathrin-coated-pit invagination, cortactin recruitment, and membrane scission observed in live cells. Cell *121*, 593-606.

Praefcke, G. J., and McMahon, H. T. (2004). The dynamin superfamily: universal membrane tubulation and fission molecules? Nat Rev Mol Cell Biol *5*, 133-147.

Qualmann, B., Kessels, M. M., and Kelly, R. B. (2000). Molecular links between endocytosis and the actin cytoskeleton. J Cell Biol *150*, F111-116.

Roux, A., Cappello, G., Cartaud, J., Prost, J., Goud, B., and Bassereau, P. (2002). A minimal system allowing tubulation with molecular motors pulling on giant liposomes. Proc Natl Acad Sci U S A *99*, 5394-5399.

Roux, A., Cuvelier, D., Nassoy, P., Prost, J., Bassereau, P., and Goud, B. (2005). Role of curvature and phase transition in lipid sorting and fission of membrane tubules. Embo J.

Sever, S., Damke, H., and Schmid, S. L. (2000). Garrotes, springs, ratchets, and whips: putting dynamin models to the test. Traffic *1*, 385-392.

Sever, S., Muhlberg, A. B., and Schmid, S. L. (1999). Impairment of dynamin's GAP domain stimulates receptor-mediated endocytosis. Nature *398*, 481-486.

Shpetner, H. S., and Vallee, R. B. (1989). Identification of dynamin, a novel mechanochemical enzyme that mediates interactions between microtubules. Cell *59*, 421-432.

Slepnev, V. I., and De Camilli, P. (2000). Accessory factors in clathrin-dependent synaptic vesicle endocytosis. Nat Rev Neurosci *1*, 161-172.

Soulet, F., Yarar, D., Leonard, M., and Schmid, S. L. (2005). SNX9 regulates dynamin assembly and is required for efficient clathrin-mediated endocytosis. Mol Biol Cell *16*, 2058-2067.

Stowell, M. H., Marks, B., Wigge, P., and McMahon, H. T. (1999). Nucleotide-dependent conformational changes in dynamin: evidence for a mechanochemical molecular spring. Nat Cell Biol *1*, 27-32.

Sweitzer, S. M., and Hinshaw, J. E. (1998). Dynamin undergoes a GTP-dependent conformational change causing vesiculation. Cell *93*, 1021-1029.

Takei, K., McPherson, P. S., Schmid, S. L., and De Camilli, P. (1995). Tubular membrane invaginations coated by dynamin rings are induced by GTP-gamma S in nerve terminals. Nature *374*, 186-190.

Takei, K., Slepnev, V. I., Haucke, V., and De Camilli, P. (1999). Functional partnership between amphiphysin and dynamin in clathrin- mediated endocytosis. Nat Cell Biol *1*, 33-39.

Tsafrir, I., Caspi, Y., Guedeau-Boudeville, M. A., Arzi, T., and Stavans, J. (2003). Budding and tubulation in highly oblate vesicles by anchored amphiphilic molecules. Phys Rev Lett *91*, 138102.

Zhang, P., and Hinshaw, J. E. (2001). Three-dimensional reconstruction of dynamin in the constricted state. Nat Cell Biol *3*, 922-926.

F-BAR Domain Purification and Mutagenesis

cDNA fragments encoding human FBP17 (1-303) and CIP4 (1-284) were subcloned into pGEX6P-1 (Amersham Biosciences, Piscataway, NJ) with codons for six additional histidine residues inserted at the C-terminus via PCR. Fusion proteins were bacterially expressed and purified first on a nickel affinity resin and then on a GST-glutathione affinity column. The GST tag was cleaved using PreScission protease (Amersham Biosciences, Piscataway, NJ), followed by gel filtration chromatography (Superdex 200 10/300 GL; Amersham Pharmacia Biosciences) in buffer containing (350 mM NaCl/250mM Imidazole/20mM HEPES/1 mM DTT, pH 7.4). Aliquots of 1-3 mg/ml protein were stored at -80° C. Site-directed mutation of select residues was performed via the quick-change protocol (Stratagene, La Jolla, CA).

Dynamin-1 Purification and Labeling

Native dynamins were purified from rat brain, and recombinant dynamin-1 was purified from baculovirus-infected SF9 cells, using the GST-tagged SH3 domain of rat amphiphysin-2 as an affinity ligand. Conjugation of dynamin to Alexa 488 or biotin was carried out by standard procedures. Unlabelled and labelled dynamins were dialysed against storage buffer (20mM HEPES, pH 7.4, 100mM NaCl, 50% (vol./vol.) glycerol), aliquoted and stored at minus 80°C.

Liposome Preparation, Membrane Binding and Tubulation *in vitro*

Synthetic lipids in chloroform were purchased from Avanti Polar Lipids and combined in mixtures composed of 85% mol./mol. phospholipids and 15% mol./mol. cholesterol. Lipids were dried under a stream of argon with gentle vortexing in glass vials, redissolved in absolute hexane, dried with argon again, and dessicated under high-vacuum for one hour. Lipids were then hydrated with buffer (50mM KCl/10mM HEPES/1mM DTT, pH 7.4), sonicated, subjected to 10 cycles of freeze-thaw, and used immediately or stored in aliquots at minus 80° C (see Fig. AII-1).

All of the results reported here for F-BAR domains, except for the mutant analysis reported below, were obtained using a synthetic phospholipid mixture that included 10% brain phosphatidyl-ethanolamine (PE), 5% liver phospho-inositides (PI), 50% palmitoyl-oleyl phosphatidyl-serine (POPS), and 35% palmitoyl-oleyl phosphatidyl-choline (POPC). Similar results, although not explicitly presented here, were also seen with synthetic phospholipid mixtures that included 20-30% brain phosphatidylethanolamine (PE), 5% liver phosphoinositides (PI), 30-40% palmitoyl-oleyl phosphatidylserine (POPS), and 35% palmitoyl-oleyl phosphatidylcholine (POPC). Finally, some of the mutants studied here (F117D in particular) only formed tubes when using liposomes composed of pure 16:0/18:1 phosphatidyl-serine (POPS). Therefore, quantitative comparisons of wild type with mutant proteins were performed after incubation with equivalent amounts of pure POPS (see below).

Liposomes (0.1 – 0.25 mg/ml) were equilibrated at 30°C (tubules) or 2°C (2D crystals) for 1 hour before adding F-BAR domains at a lipid-to-protein ratio of 2:1 mass/mass. The ability of the F-BAR domain to bind phospholipids is sensitive to salt concentration, hence protein aliquots in high salt buffers were diluted >5-fold into ddH_2O,

or protein+liposome mixtures were dialyzed against a low salt buffer overnight (50mM KCl/10mM HEPES/1mM DTT, pH 7.4) with similar results. Well-ordered helical lattices were obtained after a period of slow cooling following tubule formation at 30°C. An annealing curve programmed into a PCR machine cooled the sample by 5 degrees per hour, each followed by 5 minutes of 1 degree warming, such that after 7 hours the sample was at 2°C. This annealing procedure was only used for generating samples for cryo(electron) imaging and structure determination, and was shown to have negligible effects on the morphology of protein-free liposomes (Figure AII-1). In contrast, obtaining 2D lattices with the wild-type protein required that the lipids never be warmer than 4°C after exposure to the protein. Comparisons of mutant and wild type protein function were performed with protein samples that were purified on the same day in the same buffers and matched in concentration as assayed by SDS-PAGE and Bradford assays. To avoid bias, quantification of tubule forming ability was measured while blinded to the identity of the protein. Tubule number and length were measured with NIH ImageJ (http://rsb.info.nih.gov/ij/).

For experiments using dynamin and dynamin+BAR proteins, two lipid preparations were used: 95% brain polar lipids (BPL) plus 5%mol./mol. phosphatidylinositol-4,5-bisphosphate ($PtdIns_{4,5}P_2$), and a synthetic lipid mixture (SLM) composed of 81%mol./mol. phospholipids (30% brain phosphatidylethanolamine (PE), 5% liver phosphoinositides (PI), 30% palmitoyl-oleyl phosphatidylserine (POPS), and 35% palmitoyl-oleyl phosphatidylcholine (POPC)), 14%mol./mol. cholesterol, and 5%mol./mol. $PtdIns_{4,5}P_2$.

Figure AII-1: Protein-Free Liposome Controls

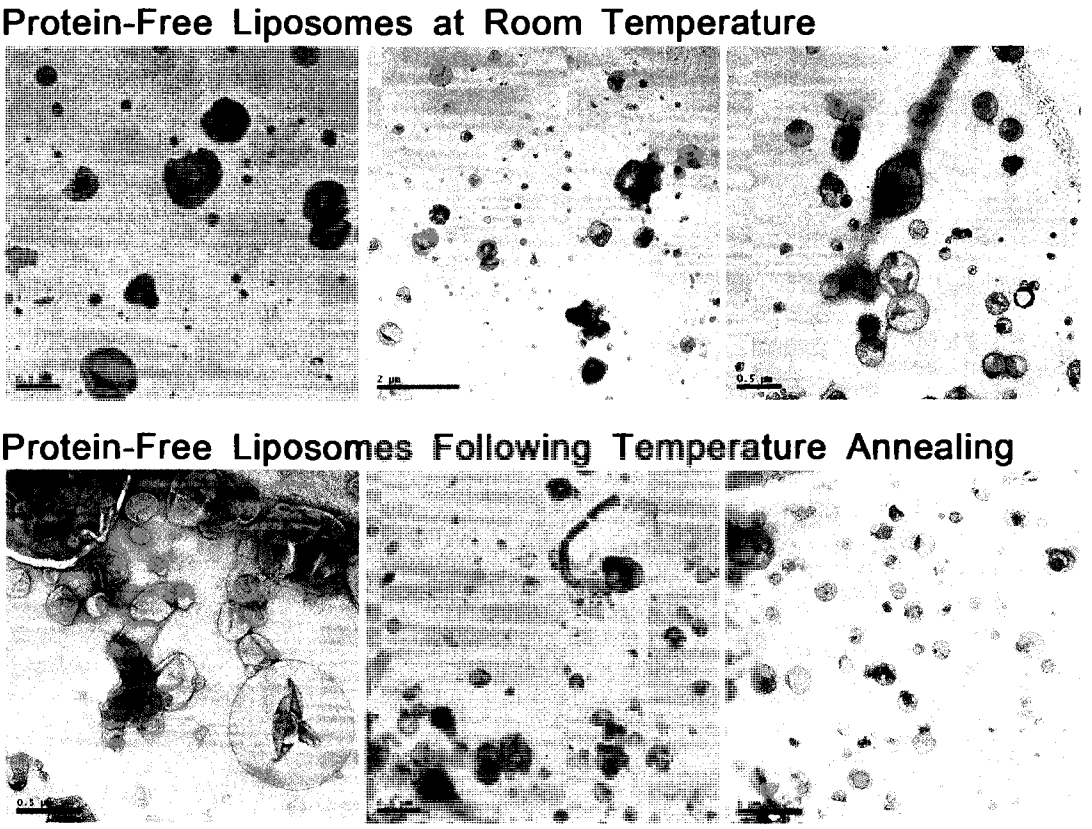

Low magnification images of a typical liposome preparation at RT, prepared by sonication and repeated cycles of freeze-thaw (top panel). Low magnification images of the same lipid preparation subjected to the temperature annealing protocol described here. Occasionally, tubular structures could be seen, but they bore no resemblance to F-BAR induced tubules (bottom panel).

Electron Microscopy

2D and helical arrays were screened and where applicable, single-axis tilt series were acquired, using 1% uranyl acetate-stained samples and a Philips Tecnai 12 microscope operating at 120 kV. To vitrify samples for cryomicroscopy, holey carbon grids were glow discharged in the presence of air, sample was applied to the grid in a cold room, and excess liquid was blotted off for 4 sec before plunging into liquid ethane. Images were taken at a sample temperature of –172°C under low-dose conditions on a Philips Tecnai F20 microscope equipped with a field emission gun and operating at an accelerating voltage of 160-200 kV, nominal magnifications of 29-50kx, and defocus values of –1,500 to –22,000 Å. Images were recorded on either Kodak SO-163 film and developed for 12 min in a full-strength Kodak D19 developer or on a GATAN 4kx4k CCD. The parameters for correction of the contrast transfer function were estimated with ACE as shown in Figure S2C (Mallick et al., 2005).

2D Crystal Image Processing

Images of 2D crystals were corrected for lattice distortions, effects of the contrast transfer function, and astigmatism using the MRC image-processing software package (Crowther et al., 1996). Two rounds of "unbending" with a Gaussian-profile maskhole were employed, with reference areas of 10% and 5% of total pixel area used in the first and second rounds, respectively. Due to the marked asymmetry of the unit cell, quantifying the anisotropy in the auto-correlation peak improved the cross-correlation map. The program ALLSPACE was used to determine whether any images of negatively stained or vitrified crystals possessed a two-dimensional plane group symmetry (Valpuesta et al., 1994). No symmetry could be found in any of the images, and attempts to average data from multiple

images in reciprocal space yielded unacceptable phase residuals. Consequently, a single-axis tilt series including 13 images from ±40° of a single negatively stained crystal was acquired. For the images of the more highly tilted crystals, the tilt angle calculated with the program EMTILT was within <1° of the nominal goniometer settings (Shaw and Hills, 1981). Applying the proper tilt geometry, all 13 images were brought to their common phase origin, merged and subjected to an additional round of origin and geometry refinement against the preliminary 3D-model obtained after fitting of the lattice lines. After fitting a final set of lattice lines (Figure AII-2) the projection structure was then calculated out of the 3D-data set using a B-factor of B=-5000Å^{-2}.

Figure AII-2: Representative Lattice Lines from 2D Crystal Tilt-Series

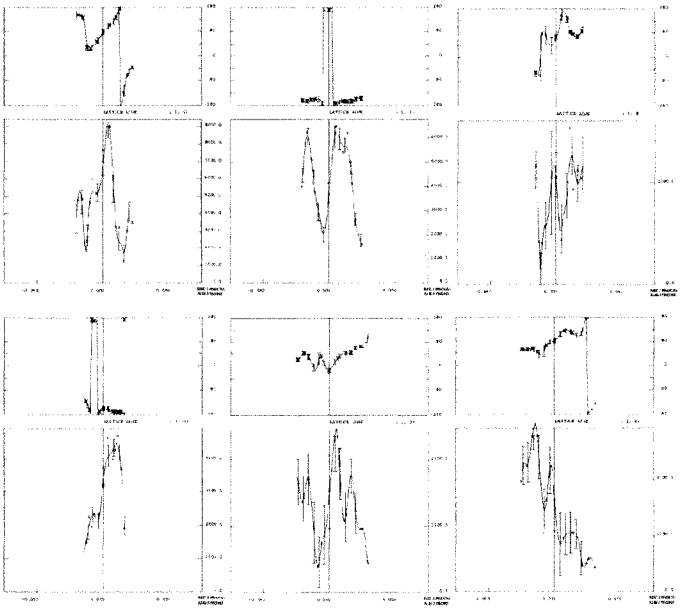

Amplitude and phase variations along representative lattice lines after merging data from tilted crystals in the plane group p1, including all reflections with a signal-to-noise ratio of >4. The continuous curves were computed by the program LATLINE (Crowther et al., 1996). The horizontal z* axis is the distance from the origin of the lattice line. Symbols in the phase plots refer to the quality of the data, as given by IQ values. Error bars are the SD of phases and amplitudes for the fitted structure factors.

Helical Image Processing

Fourier–Bessel reconstruction proved to be limited in recovering high resolution features from the large, hollow helical arrays because of flexibility and multiple image interpolations required for axis alignment and straightening (Figure AII-3). Moreover, helices with the same apparent diameter proved to have distinct helical symmetries, precluding reciprocal space averaging. We therefore reconstructed individual tubes with an extended version of the Iterative Helical Real Space Reconstruction (IHRSR) single particle algorithm as implemented in SPIDER (Egelman, 2000; Frank et al., 1996). Modifications to the procedure included the use of low-resolution Fourier-Bessel reconstructions as starting models (Figure S3A-B); initial rounds of projection matching performed with layer-line filtered images to enhance the SNR for the helical symmetry search; searching for continuous, but smoothly varying, out-of-plane tilt to identify short-range bending in the direction perpendicular to the tube's long axis (Figure S2D) and 3D CTF correction with Wiener filtering using the frequency-dependent spectral signal-to-noise ratio as determined in SPIDER (Frank et al., 1996; Pomfret et al., 2007). Each reconstruction is based on 1,200-2,400 segments, each 75 nm long with an overlap of 73 nm. The total number of unique F-BAR dimers contributing to the reconstructions ranged from ~1500 to ~3000 and the highest resolution was achieved from images of tubules with an inherent two-fold rotational symmetry, C_n=2, around the cylindrical axis (Figure AII-3). Handedness was confirmed by analysis of images acquired after tilting the specimen relative to the imaging plane. Surface renderings were created with UCSF Chimera (Pettersen et al., 2004) and CCP4MG (Potterton et al.). Evolutionary conservation scores and surface mapping were determined with Consurf (Landau et al., 2005). Resolution estimates were calculated *ab inito* with RMEASURE (Sousa and Grigorieff, 2007). Helical arc lengths along the left-handed path

defined by the lateral interactions were calculated according to: $s = \sqrt{R^2 + \left(\frac{\Delta z}{\Delta \theta}\right)^2} \bullet (\Delta \theta)$,

where R is the radius, Δz and $\Delta\theta$ are the experimentally determined rise and twist for this periodicity, respectively.

Figure AII-3: Resolution Comparison, Representative Electron (Cryo)Micrograph, Determination of CTF and Out-of-Plane Tilt

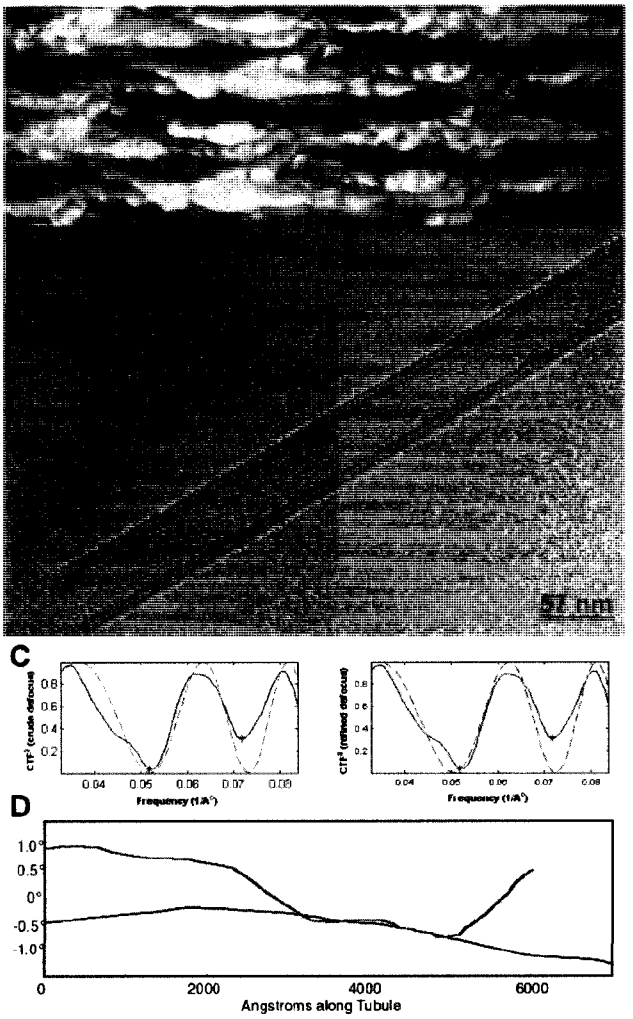

A) An atomic model of the F-BAR domain was converted to SPIDER format and filtered to 17 Å (purple) before fitting it manually into the helical reconstruction (grey), confirming that the resolution is at least as good as the ab inito estimate (Frank et al., 1996; Sousa and Grigorieff, 2007). B) A windowed region from a raw micrograph of a helical tubule taken at 160kV, revealing a broken open end. C) Representative CTF results from the program ACE (Mallick et al., 2005). D) The final reference projection libraries include images with up to 2° of out-of-plane tilt by 0.15° steps. As the particle images overlap by 97%, a moving average of the out-of-plane tilt values is plotted against position along the tubule length for two representative tubules.

Figure AII-4: Fourier-Bessel Reconstructions from Individual Tubules & the Presence of Rotational Symmetry.

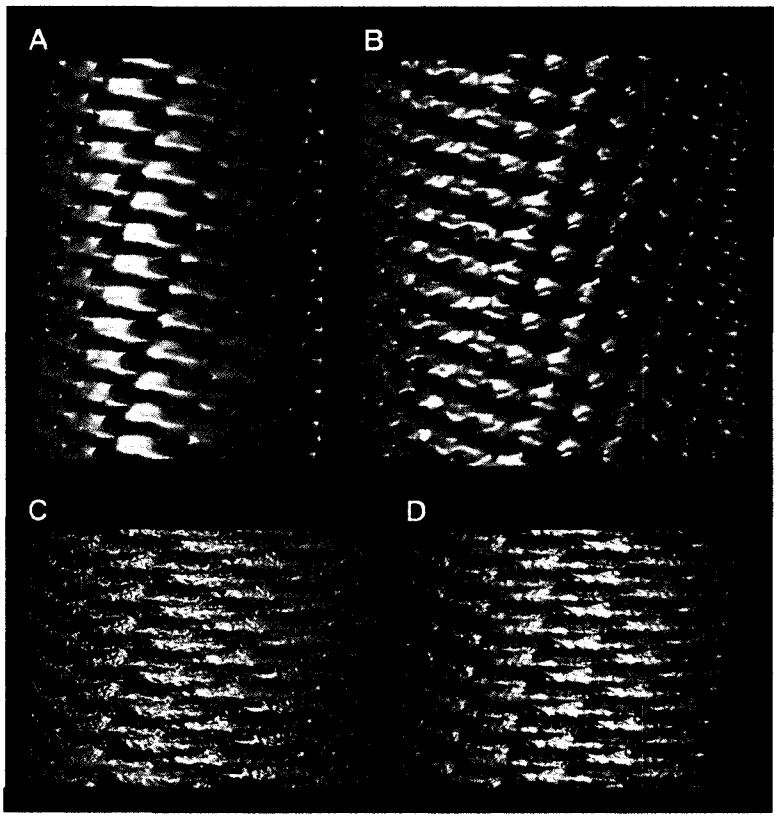

A,B) Volumes calculated via Fourier-Bessel inversion for a narrow (A) and a wide tubule (B) (Carragher et al., 1996). These volumes were used as starting models for single particle iterative helical reconstructions. C,D) The reconstruction shown in Figures 3-4 without (A) versus with (B) imposition of the 2-fold rotational symmetry.

Cell culture, transfection and reagents (R. Perera)

COS7 cells (ATCC, Rockville, MD) were cultured at 37°C and 5% CO_2 in Dulbecco's modified Eagle's medium supplemented with 10% fetal bovine serum. FBP17-GFP, mRFP-FBP17 and Amphiphysin2-GFP have all been previously described (Itoh et al.,

2005). GFP- and mRFP-tagged proteins were co-expressed in COS7 cells by transfecting 1-3μg DNA using the Amaxa nucleofector kit (Amaxa, Cologne, Germany). Cells were seeded in glass-bottomed 35mm dishes (Mattek Corporation, Ashland, MA) and imaged approximately 14-24 hours later (50-70% confluency). For immunofluorescence, cells were grown on coverslips, fixed with 4% formaldehyde (freshly prepared from parafomaldehyde), and processed by standard procedures.

Live Cell Microscopy (R. Perera)

Prior to imaging, medium was replaced with an imaging buffer containing 136mM NaCl, 2.5mM KCl, 2mM $CaCl_2$, 1.3mM $MgCl_2$, 10mM HEPES at pH 7.4. Cells were imaged at 37°C using a spinning-disk confocal system (Perkin Elmer, Waltham, MA), mounted onto an IX-71 inverted microscope (Olympus, Melville, NY), equipped with a 1Kb x 1Kb, Hamamatsu EM-CCD camera (Hamamatsu, Hamamatsu City, Japan). Samples were imaged using a 100X oil objective, yielding a spatial resolution of 0.1 μm/pixels. Excitation was achieved using 488 argon and 568 argon/krypton lasers (Melles Griot, Carlsbad, CA). Exposure times were between 0.2-0.6 seconds. NIH Image J and/or iQ software was used to process raw images.

Formation of Membrane Sheets (A. Roux)

A pre-washed glass coverslip stored in ethanol was dried under a N_2 flux, and 1 ml droplets of lipid solution (10 mg/ml 2:1 in pure chloroform) were deposited and allowed to dry on the coverslip. Lipid-coated coverslips were further dried under vacuum for at least one hour. A small chamber was built by placing the coverslip onto a glass slide, with the

lipids facing the glass slide, using double-sided tape as spacers. The lipids were fully re-hydrated by filling the chamber by capillary action with 15–20 ml of buffer.

Fig. AII-5: The experimental system used to analyze the tubulation of lipid bilayers by differential interference contrast (DIC) microscopy. Lipids are spotted in a small chamber between surfaces, dried, and then rehydrated to generate sheets, typically composed few superimposed layers. Protein-containing solutions are added to the chamber during

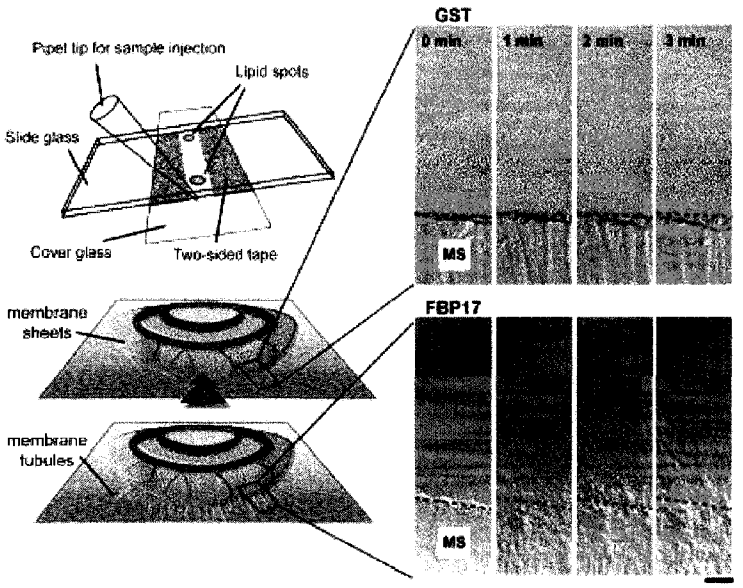

diagram of a lipid spot before and after application of a tubulating protein. Right: Time course analysis of edges of membrane sheets (MS) during the incubation with a control protein (top) or with FBP17 (bottom). Scale bar = 5 μm. Figure and legend taken from (Itoh et al., 2005). The experimental method and this figure were created by Aurélin Roux.

Video-DIC and Determination of Persistence Lengths (A. Roux)

Membrane preparations were placed on the stage of an Axiovert 200 ZEISS (Germany) microscope for observation at room temperature with a JAI Pulnix (USA) TM1400CL camera and DVR software (Advanced Digital Vision Inc. USA). FBP17, amphiphysin and dynamin containing solutions were applied to one side of the chamber and the deformation of membrane sheets produced by its diffusion into the chamber was

recorded at normal video rate (30 fps) with 1300x1024 resolution under Differential Interference Contrast (DIC) settings (Itoh et al., 2005; Roux et al., 2006). For each tubule, positions of the tip and the base were tracked using the manual tracking plugin with NIH ImageJ (http://rsb.info.nih.gov/ij/). This procedure was repeated for one hundred sequential frames for each tubule, and the tip-to-base distance was extracted for each frame. Each data point is the rms^2 (root mean square to the square) for all of the tip-to-base measurements for a given tubule. The rms^2 were plotted against the total length and the theoretical curve fit to the data derives from the following equation: $\delta R^2(t) = 2(L_p)^2[x/L_p - 1 + e^{(-x L_p)}]$; where $\delta R^2(t)$ is the rms^2, x the total length and L_p the persistence length (Derenyi et al., 2002; Le Goff et al., 2002a; Le Goff et al., 2002b).

Kinesin-induced lipid tubulation (A. Roux)

Microtubule-coated chambers between glass-slides were prepared as described (Roux et al., 2002), but using double sided tape as the spacer and washed with kinesin motility buffer (see below). Giant liposomes were generated using modifications of the protocol from (Moscho et al., 1996). One mg of BPL supplemented with 5% PtdIns(4,5)P_2 and 5% biotin-LC-DOPE lipid (Avanti Polar Lipids, USA) was dried in a glass vial under vacuum for at least half an hour. Lipids were re-suspended by vortexing for 5 min in 1 ml GTPase buffer containing 1% v/v glycerol. Small unilamellar vesicles were obtained by sonicating the solution on ice with a tip sonicator for 5 min (0.3 Hz cycles) and stored at –20°C. For the experiments, 5 µl of solution were spotted and dried on a glass slide in the vacuum oven for half an hour. Giant liposomes were obtained by re-hydrating the lipid spot for 10-15 min with 10 µl 220 mM sucrose. These liposomes were then carefully aspirated from the glass slide surface with a micropipette, transferred to an Eppendorf tube, clarified by mixing with

GTPase buffer (100 μl final volume) and spun at 800 rpm for 2 min. The top 50 μl of the solution were replaced by fresh GTPase buffer and, after resuspension, this material was further spun at 800 rpm for 2 min. The top 75 μl were discarded and the remaining material (giant liposomes) was used as follows as starting material for the generation of kinesin-pulled tubules. 3 μl of giant liposomes were mixed with 2 μl of 0.1 mg/ml streptavidin in GTPase buffer and incubated for 3 min. Two μl of biotinylated recombinant drosophila kinesin (typically from a 1 μM stock, cDNA for was kind gift of Patricia Bassereau, Institut Curie, Paris) was then added to this mixture, incubated for 5 min and added to 7 μl of motility buffer (2 mM ATP, 0.4 mg/ml glucose oxidase, 0.2 mg/ml catalase, 240 mM glucose, 5 mM DTT, 10 μM taxol, in GTPase Buffer). The resulting material was added to the microtubule-coated microchambers after their prewashing with 20 μl of motility buffer. After a 15-20 min incubation to allow tubules to grow, 5 μl of Alexa 488-dynamin in GTPase buffer were applied to the chamber. Following an additional 15-20 incubation, 5 μl 1mM GTP in GTPase buffer were applied.

Wide-Angle X-Ray Scattering

Liposomes at 20mg/ml were sealed into thin-walled glass capillaries that were thermally equilibrated at 30°C or 4°C for 30 minutes before data acquisition. X-ray diffractograms were recorded with an image plate mounted on a sealed-tube Rigaku R-Axis IIC operating at 50 kV and 100 mA. The x-ray beam was filtered for CuKα radiation using a Ni foil. Diffraction patterns were recorded at each temperature for 10 to 30 min.

Thin Section TEM

COS7 cells were fixed with either 1.3% glutaraldehyde in 66mM sodium cacodylate buffer or 2% glutaraldehyde in a buffer containing 30mM Hepes-NaOH (pH 7.4), 100mM NaCl, 2.5mM $CaCl_2$. Subsequently, they were post-fixed with 1% OsO_4 in 1.5% $K_4Fe(CN)_6$ and 0.1M sodium cacodylate, en bloc stained with 0.5% uranyl magnesium acetate, dehydrated and embedded in Embed 812. Sections were imaged in a Philips Tecnai 12 operating at 120 kV. Electron microscopy reagents were purchased from Electron Microscopy Sciences (Hatfield, PA).

References

Carragher, B., Whittaker, M., and Milligan, R. A. (1996). Helical Processing Using PHOELIX. Journal of Structural Biology *116*, 107-112.

Crowther, R. A., Henderson, R., and Smith, J. M. (1996). MRC image processing programs. J Struct Biol *116*, 9-16.

Derenyi, I., Julicher, F., and Prost, J. (2002). Formation and interaction of membrane tubes. Phys Rev Lett *88*, 238101.

Egelman, E. (2000). A robust algorithm for the reconstruction of helical filaments using single-particle methods. Ultramicroscopy *85*, 225-234.

Frank, J., Radermacher, M., Penczek, P., Zhu, J., Li, Y., Ladjadj, M., and Leith, A. (1996). SPIDER and WEB: processing and visualization of images in 3D electron microscopy and related fields. J Struct Biol *116*, 190-199.

Itoh, T., Erdmann, K., Roux, A., Habermann, B., Werner, H., and De Camilli, P. (2005). Dynamin and the actin cytoskeleton cooperatively regulate plasma membrane invagination by BAR and F-BAR proteins. Dev Cell *9*, 791–804.

Landau, M., Mayrose, I., Rosenberg, Y., Glaser, F., Martz, E., Pupko, T., and Ben-Tal, N. (2005). ConSurf: identification of functional regions in proteins by surface-mapping of phylogenetic information. Nucleic Acids Res *33*, W299-W302.

Le Goff, L., Amblard, F., and Furst, E. M. (2002a). Motor-driven dynamics in actin-myosin networks. Phys Rev Lett *88*, 018101.

Le Goff, L., Hallatschek, O., Frey, E., and Amblard, F. (2002b). Tracer studies on f-actin fluctuations. Phys Rev Lett *89*, 258101.

Mallick, S. P., Carragher, B., Potter, C. S., and Kriegman, D. J. (2005). ACE: Automated CTF Estimation. Ultramicroscopy *104*, 8-29.

Moscho, A., Orwar, O., Chiu, D., Modi, B., and Zare, R. (1996). Rapid Preparation of Giant Unilamellar Vesicles. Proceedings of the National Academy of Sciences of the United States of America *93*, 11443-11447.

Pettersen, E., Goddard, T., Huang, C., Couch, G., Greenblatt, D., Meng, E., and Ferrin, T. (2004). UCSF Chimera—A visualization system for exploratory research and analysis. Journal of Computational Chemistry *25*, 1605-1612.

Pomfret, A. J., Rice, W. J., and Stokes, D. L. (2007). Application of the iterative helical real-space reconstruction method to large membranous tubular crystals of P-type ATPases. J Struct Biol *157*, 106-116.

Potterton, L., McNicholas, S., Krissinel, E., Gruber, J., Cowtan, K., Emsley, P., Murshudov, G., Cohen, S., Perrakis, A., and Noble, M. Developments in the CCP 4 molecular-graphics project. logo *60*, 2288-2294.

Roux, A., Cappello, G., Cartaud, J., Prost, J., Goud, B., and Bassereau, P. (2002). A minimal system allowing tubulation with molecular motors pulling on giant liposomes. Proc Natl Acad Sci U S A *99*, 5394-5399.

Roux, A., Uyhazi, K., Frost, A., and De Camilli, P. (2006). GTP-dependent twisting of dynamin implicates constriction and tension in membrane fission. Nature *441*, 528-531.

Shaw, P., and Hills, G. (1981). Tilted specimen in the electron microscope: a simple specimen holder and the calculation of tilt angles for crystalline specimens. Micron *12*, 279-282.

Sousa, D., and Grigorieff, N. (2007). Ab initio resolution measurement for single particle structures. J Struct Biol *157*, 201-210.

Valpuesta, J. M., Carrascosa, J. L., and Henderson, R. (1994). Analysis of electron microscope images and electron diffraction patterns of thin crystals of phi 29 connectors in ice. J Mol Biol *240*, 281-287.